Anticipating a new physics signal in upcoming 21-cm power spectrum observations

Rennan Barkana®, ^{1,2,3,*} Anastasia Fialkov®, ^{4,5,†} Hongwan Liu®, ^{6,7,‡} and Nadav Joseph Outmezguine® ^{8,9,§}

¹School of Physics and Astronomy, Tel-Aviv University, Tel-Aviv, 69978, Israel

²Institute for Advanced Study, 1 Einstein Drive, Princeton, New Jersey 08540, USA

³Department of Astronomy and Astrophysics, University of California, Santa Cruz, California 95064, USA

⁴Institute of Astronomy, University of Cambridge, Madingley Road,

Cambridge, CB3 0HA, United Kingdom

⁵Kavli Institute for Cosmology, Madingley Road, Cambridge CB3 0HA, United Kingdom

⁶Center for Cosmology and Particle Physics, Department of Physics, New York University,

New York, New York 10003, USA

⁷Department of Physics, Princeton University, Princeton, New Jersey, 08544, USA

⁸Berkeley Center for Theoretical Physics, University of California, Berkeley, California 94720, USA

⁹Theory Group, Lawrence Berkeley National Laboratory, Berkeley, California 94720, USA

(Received 17 January 2023; accepted 9 August 2023; published 7 September 2023)

Dark matter–baryon interactions can cool the baryonic fluid, which has been shown to modify the cosmological 21-cm global signal. We show that in a two-component dark sector with an interacting millicharged component, dark matter–baryon scattering can produce a 21-cm power spectrum signal with acoustic oscillations. The signal can be up to 3 orders of magnitude larger than expected in ΛCDM cosmology, given realistic astrophysical models. This model provides a new-physics target for near-future experiments such as HERA or NenuFAR, which can potentially discover or strongly constrain the dark matter explanation of the putative EDGES anomaly.

DOI: 10.1103/PhysRevD.108.063503

I. INTRODUCTION

In recent years, rapid progress has been made toward turning 21-cm cosmology into reality, opening a valuable window into the Universe at $6 \lesssim z \lesssim 30$. During this epoch, the intergalactic medium (IGM) reached its lowest temperature in cosmological history, before heating up due to star formation, which began in dark matter (DM) halos of sufficient mass. As a result, 21-cm measurements probe the previously unknown period of cosmic dawn and the first stars [1–5], and are particularly sensitive to new-physics processes that impact the thermal state of the IGM or the process of star formation during this epoch [6–32].

The observable in 21-cm cosmology is the brightness temperature of radiation with wavelength 21 cm, T_{21} , absorbed or emitted by the hyperfine states of neutral

Published by the American Physical Society under the terms of the Creative Commons Attribution 4.0 International license. Further distribution of this work must maintain attribution to the author(s) and the published article's title, journal citation, and DOI. Funded by SCOAP³. hydrogen atoms, and observed at a redshifted wavelength. Measurements of the sky-averaged T_{21} (i.e., the global 21-cm signal) have generated significant excitement in recent years. The EDGES Collaboration reported a detection of the global signal [33], finding a large absorption trough of $-0.5^{+0.2}_{-0.5}$ K at $z\sim17$ at 99% confidence. This result is in significant tension with expectations from ΛCDM cosmology [20]. More recently, however, the SARAS experiment found that the central value of the EDGES absorption profile is inconsistent with their measurements at 95% confidence [34]. It is worth noting that 21-cm experiments face severe observational hurdles, which may take several years of scrutiny to resolve. The discrepancy observed in the EDGES experiment, for instance, has often been attributed to potential systematic uncertainties rather than a new physical phenomenon [35-39]. Near-future global signal experiments such as PRIZM [40], SCI-HI [41], REACH [42], and MIST [43], as well as future results from EDGES and SARAS will help to clarify the situation soon.

Meanwhile, T_{21} power spectrum measurements have been improving steadily. Over the last decade, experiments such as GMRT [44], MWA [45–50], LOFAR [51,52], PAPER [53], LEDA [54], and HERA [55,56] have set increasingly strong upper limits on the power spectrum for comoving wave numbers 0.03–3 Mpc⁻¹, in a broad redshift

^{*}barkana@tau.ac.il

[†]anastasia.fialkov@gmail.com

[†]hongwanl@princeton.edu

[§]njo@berkeley.edu

range of $6 \lesssim z \lesssim 17$; current limits are potentially 1 order of magnitude away from optimistic Λ CDM expectations [57]. Alongside these advancements, the MeerKAT experiment has recently reported a notable first detection of the 21-cm power spectrum at low redshifts, indicating a promising direction for 21-cm cosmology [58].

Inspired by the EDGES result, recent effort has been directed toward finding models that enhance the global signal. This can be accomplished by either increasing the brightness of the background radiation [33,59–63], or by reducing the baryon temperature [13-19], typically through DM-baryon scattering [20–32]. In this paper, we revisit the two-fluid dark sector—comprising a dominant cold DM (CDM) and a subdominant millicharged DM (mDM)—first presented in Ref. [29]. This model generates a large global signal absorption trough by cooling baryons efficiently, without introducing significant drag on the baryonic fluid in the early Universe. Here, we show that the same model also leads to an enhanced power spectrum that can be several orders of magnitude larger than ACDM expectations. A strong correlation between baryon temperature and the baryon-DM bulk relative velocity naturally imprints large acoustic oscillations on the signal [20,22,25], with a much larger amplitude than is possible through the effect on galaxy formation in standard astrophysical models [3,27,64–67]. An oscillation signature is possible in principle within the simpler, noninteracting millicharged DM model [23,27], but it is erased by drag at early times throughout the small parameter space of this model that remains consistent with observational constraints, particularly the constraints from the cosmic microwave background (CMB) [28,68,69]. The predicted power spectrum in the interacting millicharged DM model provides a nearfuture, new-physics target for 21-cm power spectrum experiments as their sensitivity improves.

II. 21-CM COSMOLOGY

As background radiation photons pass through a region of neutral hydrogen, they interact with the hydrogen hyperfine states. Consequently, absorption, spontaneous emission and stimulated emission of 21-cm photons change the background radiation intensity at that wavelength. The photon intensity then redshifts; the temperature contrast between the transmitted radiation and the background radiation, observed today at a wavelength 21(1+z) cm, is referred to as the 21-cm brightness temperature and denoted by $T_{21}(z)$. We assume throughout this paper that the background radiation temperature is the CMB temperature, $T_{\gamma}(z) = 2.725(1+z)$ K. T_{21} is determined by the spin temperature T_{S} of neutral hydrogen gas, via [1,4,5]

$$T_{21}(z) \simeq \frac{1}{1+z} [T_{S}(z) - T_{\gamma}(z)][1 - e^{-\tau(z)}],$$
 (1)

where $\tau(z)$ is the effective optical depth of photons with wavelength of 21 cm at redshift z.

 $T_{\rm S}$ is determined by the interaction of neutral hydrogen atoms with (1) the CMB photons at temperature T_{γ} , (2) other hydrogen atoms in the gas with temperature $T_{\rm b}$, and (3) Lyman- α (Ly α) radiation, which influences $T_{\rm S}$ through the Wouthuysen-Field (WF) effect [70,71]. The first process drives $T_{\rm S} \to T_{\gamma}$, while the other two processes pull $T_{\rm S} \to T_{\rm b}$ instead; as a result, $T_{\rm S}$ takes a value between T_{γ} and $T_{\rm b}$. The relative strength of these processes can be parametrized by a single coupling coefficient $x_{\rm tot,eff}$, encapsulating the collisional and Ly α interactions [5],

$$T_{\rm S}^{-1}(\mathbf{x}, z) = \frac{T_{\gamma}^{-1}(z) + x_{\rm tot,eff}(\mathbf{x}, z) T_{\rm b}^{-1}(\mathbf{x}, z)}{1 + x_{\rm tot,eff}(\mathbf{x}, z)},$$
(2)

where we have also introduced the spatial (x) dependence of $T_{\rm S}$, resulting from inhomogeneities in $T_{\rm b}$ and $x_{\rm tot,eff}$. Further details on the value of $x_{\rm tot,eff}$ and other details of the calculation of T_{21} are discussed in Appendix B.

There are two main types of 21-cm observables. The first is the global or sky-averaged brightness temperature, which we denote by $\langle T_{21}\rangle(z)$. After the first stars formed and started emitting significant Ly α radiation at $z\lesssim 25$, but prior to substantial x-ray heating of the IGM at $z\lesssim 15$, $T_{\rm b}\leq T_{\rm S}\leq T_{\gamma}$, leading to a global signal that is in absorption, i.e., $\langle T_{21}\rangle\leq 0$. A value of $\langle T_{21}\rangle(z=17)$ no lower than approximately -150 mK is expected within Λ CDM cosmology [57].

The second observable is the power spectrum of spatial fluctuations in the brightness temperature, $P_{T_{21}}(k,z)$, which is a function of comoving wave number k and redshift z. The dimensionless power spectrum $P_{T_{21}}/\langle T_{21}\rangle^2$ is the Fourier transform of the two-point correlation function (2PCF) of fluctuations, $\xi_{T_{21}}(\mathbf{x}) = \langle \delta_{T_{21}}(\mathbf{x}_1)\delta_{T_{21}}(\mathbf{x}_2)\rangle_{\mathbf{x}}$, where $\langle \cdots \rangle_{\mathbf{x}}$ denotes a spatial average over all pairs of points \mathbf{x}_1 and \mathbf{x}_2 such that $\mathbf{x} = \mathbf{x}_1 - \mathbf{x}_2$, and where $\delta_{T_{21}} \equiv T_{21}/\langle T_{21}\rangle - 1$. For our isotropic Universe, $\xi_{T_{21}}$ is a function only of $\mathbf{x} \equiv |\mathbf{x}|$ and $P_{T_{21}}$ can be written as

$$\frac{P_{T_{21}}(k,z)}{\langle T_{21} \rangle^2(z)} = 4\pi \int_0^\infty dx x^2 \xi_{T_{21}}(x,z) \frac{\sin(kx)}{kx}.$$
 (3)

 $P_{T_{21}}$ is often equivalently expressed in terms of the power per $\log k$, $\Delta_{21}^2(k,z) \equiv k^3 P_{T_{21}}(k,z)/(2\pi^2)$.

III. TWO-FLUID DARK SECTOR

The two-fluid interacting millicharged DM model, first proposed in Ref. [29], is capable of cooling baryons during the cosmic dark ages sufficiently to produce a global signal $\langle T_{21} \rangle (z=17)$ consistent with the EDGES result, while avoiding stringent CMB constraints on momentum transfer between baryons and dark matter [28,69,72–74].

To accomplish this, the dark sector comprises two components: a millicharged component (mDM) with mass $m_{\rm m}$ and electric charge Q that makes up $f_{\rm m} \lesssim 4 \times 10^{-3}$ of the total DM energy density, and a cold component (CDM) which accounts for the remainder. A light mediator between mDM and CDM allows for energy transfer between these two fluids.

Prior to recombination, the mDM electric charge and mDM-CDM couplings are set such that the mDM fluid is tightly coupled to the baryons. After recombination, the baryonic fluid becomes mostly neutral; as a result, the mDM fluid decouples from the baryons, and instead becomes coupled to the CDM fluid, which has a temperature below the baryon temperature at all times. The mDM-baryon interactions now transfer heat from the baryons to the entire CDM-mDM fluid, cooling $T_{\rm b}$ well below the Λ CDM expectation. The tight mDM-CDM coupling allows for heat flowing from the baryonic fluid to be shared among all dark-sector particles, greatly enhancing the available heat capacity for cooling.

The most compelling particle physics models allowing particles to carry a small electrical charge also require the existence of a light "hidden photon" [75]. We note that this hidden photon is not the light mediator allowing the heat transfer between mDM and CDM. To avoid CMB $N_{\rm eff}$ limits on a combination of millicharged particles and light hidden photons, in this paper we focus on $m_{\rm m} \gtrsim 1~{\rm GeV}$, which is sufficiently massive to avoid the constraints of Ref. [32].

As in the ΛCDM paradigm, baryon acoustic oscillations set up a local bulk relative velocity between the baryons (together with the mDM) and CDM, $v_{bC}(x)$, with a rootmean-square velocity of $v_{\rm rms} \equiv \langle v_{\rm bC}^2(\mathbf{x}) \rangle^{1/2} \approx 29 \text{ km s}^{-1}$ at z = 1010 [3]. Unlike the noninteracting millicharged DM model [23], the mDM-CDM coupling in the interacting model restores the mDM-baryon velocity difference after cosmic recombination. Since the mDM-baryon interaction responsible for heat transfer from the baryons weakens rapidly with velocity, patches with large initial $v_{\rm bC}$ remain hotter than the rapidly cooling patches with vanishing $v_{\rm bC}$ [20,22]. This is an important point: the relative bulk motion at $z \sim 1010$ results in different initial conditions for the baryon temperature evolution at each spatial location. This spatial variation in $T_{\rm b}$ leads to spatial variation in the brightness temperature T_{21} through Eqs. (1) and (2). In particular, the correlation with $v_{\rm bC}$ imprints the acoustic oscillations in the $v_{\rm bC}$ power spectrum onto the 21-cm power spectrum [3,20].

Following Ref. [29], we compute $T_{\rm b}$ as a function of dark matter parameters Q and $m_{\rm m}$, fixing the CDM mass at $m_{\rm C}=100$ MeV and also $f_{\rm m}=10^{-4}$. Varying 10 MeV $\lesssim m_{\rm C}\lesssim 18$ GeV and $10^{-8}\lesssim f_{\rm m}\lesssim 4\times 10^{-3}$ changes the required values of $m_{\rm m}$ and Q to get significant cooling of the baryonic fluid, but otherwise does not qualitatively change our results [29]. We choose the maximal coupling

between mDM and CDM, permitting both tight coupling between mDM and baryons before recombination, and a sufficiently small drag on the baryonic fluid to avoid CMB power spectrum constraints [28,69] (see also Appendix C of Ref. [29]). We integrate the differential equations governing the properties of the mDM, CDM and baryon fluids starting from photon decoupling at z=1010, for various initial bulk velocities $v_{\rm bC}$, ultimately obtaining $T_{\rm b}(Q,m_{\rm m};v_{\rm bC};z)$.

IV. ASTROPHYSICS MODELING

To relate $T_{\rm b}(Q, m_{\rm m}; v_{\rm bC}, z)$ from our model to a value of $T_{21}(Q, m_{\rm m}; v_{\rm bC}, z)$ through Eqs. (1) and (2), we need an astrophysical model for the Ly α and x-ray radiation fields. Ly α photons determine the coupling of T_S to T_b in Eq. (2), while both Ly α and x-ray photons lead to IGM heating, partially counteracting cooling by mDM. To determine both of these effects, we rely on a large-scale, seminumerical 21-cm code based on Refs. [57,66,76]. In this paper, we aim to highlight the discovery potential of the two-fluid dark sector model in the 21-cm power spectrum; we therefore account for the minimal effect of realistic astrophysical models. This contrasts with the typically adopted simplistic approach that derives the maximum possible signal by assuming no astrophysical heating together with full Ly α coupling (i.e., $x_{\text{tot,eff}} \rightarrow \infty$); in practice, this limit is not possible, since strong Ly α coupling brings along with it significant heating, thus narrowing the range of possible 21-cm signals [57]. We use an ensemble of 140 realistic astrophysical models from the seminumerical simulations, chosen to minimize astrophysical heating and maximize Ly α coupling. As shown below, we must use an ensemble since the astrophysical model that gives the maximum absorption of T_{21} depends on the DM parameters and on redshift. Further details on the simulations and the astrophysical parameters are discussed in Appendix D.

As we focus on models with subdominant x-ray heating, the dominant process counteracting dark cooling is Ly\$\alpha\$ heating. Ly\$\alpha\$ heating results from the scattering of Ly\$\alpha\$ photons, either directly from atomic recoil [77–79], or by mediating heat transfer from the CMB to the baryons [80]. From each simulation, we obtain the spatially averaged baryon temperature $\Theta_b^A(z)$, with A indexing the 140 simulated astrophysical models (we use Θ to denote temperatures that are spatially averaged and T for temperatures that vary over space through v_{bC} for clarity). To account for astrophysical heating in our calculations we define the excess heating as $\delta \Theta_b^A(z) \equiv \Theta_b^A(z) - \Theta_b^0(z)$, where $\Theta_b^0(z)$ is the Λ CDM prediction for the baryon temperature in the absence of heating. The final baryon temperature is then

$$T_{\rm b}^{A}(Q, m_{\rm m}; v_{\rm bC}; z) = T_{\rm b}(Q, m_{\rm m}; v_{\rm bC}; z) + \delta\Theta_{\rm b}^{A}(z)$$
 (4)

for each astrophysical model. The second ingredient we obtain from each simulation is the average effective coupling $x_{\text{tot,eff}}^A(T_b;z)$ from the spatially averaged Ly α radiation field. $T_{21}^A(Q,m_{\text{m}};v_{\text{bC}};z)$ is then determined by substituting $x_{\text{tot,eff}}^A(T_b;z)$ into Eq. (2) together with Eq. (4).

Note that we have ignored spatial variations in $\delta\Theta_b^A$, as well as in the Ly α radiation field, using only their mean values, and thus leaving the dependence of T_b on v_{bC} as the only source of fluctuations. While a fully self-consistent treatment including astrophysical heating and dark cooling would account for all spatial variations concurrently, the simplified prescription presented here is computationally much more feasible, and is a reasonable approximation within the parameter range of interest, for which the effect of velocity fluctuations strongly dominate.

V. BULK RELATIVE VELOCITY

In the two-fluid interacting dark-sector model, the fluctuations of T_{21} are set primarily by the dependence of the baryon temperature on $v_{\rm bC}$. This correlates the spatial variations of T_{21} (at any redshift), to those of $v_{\rm bC}$ at $z\sim 1010$, assuming that any other sources of such fluctuations are subdominant.

Since the drag between the baryons and CDM is small, v_{bC} at recombination is as it is in the Λ CDM paradigm: a Gaussian random field with a power spectrum $P_v(k)$ defined through $\langle \tilde{v}_{bC}(\pmb{k}) \tilde{v}_{bC}(\pmb{k}') \rangle = (2\pi)^3 \delta^{(3)}(\pmb{k} + \pmb{k}') P_v(k)$, where $\hat{\pmb{k}} \tilde{v}_{bC}(\pmb{k}) \equiv \tilde{v}_{bC}(\pmb{k})$, the Fourier transform of $v_{bC}(\pmb{x})$. $P_v(k)$ exhibits the characteristic acoustic oscillations in k [3].

Under our assumption that the spatial fluctuations of T_{21} are dominated by its dependence on $v_{\rm bC}$, the global signal is evaluated as

$$\langle T_{21} \rangle = \left(\frac{3}{2\pi v_{\rm rms}^2} \right)^{3/2} \int d^3 v_{\rm bC} T_{21}(v_{\rm bC}) \exp\left(-\frac{3v_{\rm bC}^2}{2v_{\rm rms}^2} \right).$$
 (5)

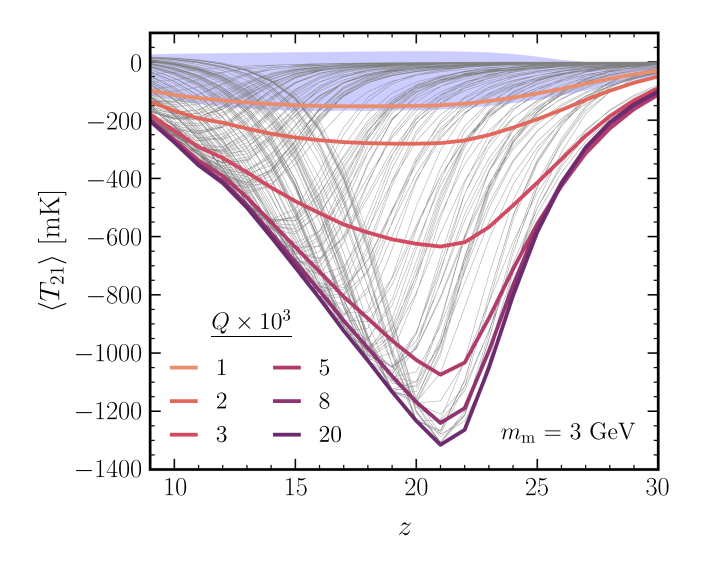
Similarly, the T_{21} 2PCF is given by

$$\xi_{T_{21}}(\mathbf{x}) = \int d^3 \mathbf{v}_{bC,a} \int d^3 \mathbf{v}_{bC,b} \times \mathcal{P}(\mathbf{v}_{bC,a}, \mathbf{v}_{bC,b}; \mathbf{x}) \delta_{T_{21}}(v_{bC,a}) \delta_{T_{21}}(v_{bC,b}),$$
(6)

where $\mathcal{P}(v_{bC,a}, v_{bC,b}; x)$ is the joint probability density function (PDF) of 3D bulk relative velocities at points a and b separated by a vector x. Since v_{bC} is a Gaussian random field, \mathcal{P} is completely specified by $P_v(k)$. In the Appendix C, we specify the exact structure of \mathcal{P} , and explain the details of our computation of $\xi_{T_{21}}$. In particular, we improve on previous results [64,81] by reducing the 6D integral in Eq. (6) to a 3D integral instead of a 4D one, making the integral much easier to evaluate numerically. The power spectrum is then calculated through Eq. (3).

VI. RESULTS

Figure 1 shows the predicted $\langle T_{21} \rangle$ and Δ_{21}^2 for comoving wave number $k=0.13~{\rm Mpc^{-1}}$ for the two-fluid interacting millicharged DM model with $m_{\rm m}=3~{\rm GeV}$, for a range of Q values that are viable given current constraints. To indicate the most easily observable models, we plot lines



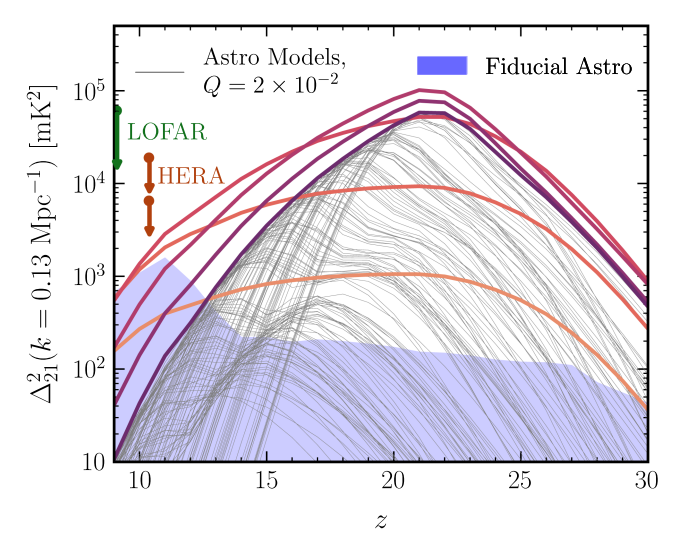


FIG. 1. Left: the minimum envelope (i.e., maximum absorption) of the predicted global signal $\langle T_{21} \rangle$ for $m_{\rm m}=3$ GeV across all astrophysical models, for various values of the charge (colored lines). Right: the maximum envelope of the power spectrum Δ_{21}^2 at k=0.13 Mpc⁻¹ for the same values of the charge (colored lines). Existing upper limits over a range of redshifts reported by LOFAR [51,52] (green), and HERA [55,56] (orange) are shown as arrows. In both panels, the signals for all astrophysical models for $Q=2\times 10^{-2}$ are shown in gray; the fiducial range of both quantities expected in standard Λ CDM cosmology is shaded in purple [57].

in color representing the minimum $\langle T_{21} \rangle$ and maximum Δ_{21}^2 envelopes, obtained by varying over all 140 astrophysical models. To give a sense of the variability in these models, we show in gray lines the 140 different models considered for the fixed value $Q=2\times 10^{-2}$. The full fiducial range of values that are possible in standard Λ CDM cosmology are shaded in purple. See Appendix A for a similar plot of Δ_{21}^2 for other values of k.

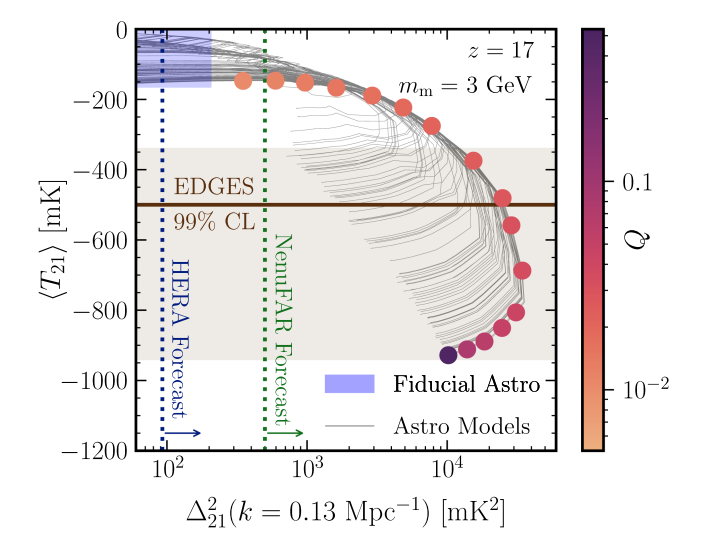
The global signal shown on the left has the characteristic absorption profile, corresponding to Ly α emission driving $T_{\rm S} \to T_{\rm b}$ before heating of the IGM causes $T_{\rm b}$ to increase; by adding x-ray heating it is possible to vary the shape further. As pointed out in Ref. [29], the global signal from our model can attain the central value of the EDGES absorption profile at z=17, producing signals as large as $\langle T_{21} \rangle (z=21) \sim -1250$ mK.

The power spectrum shown on the right is predicted to reach $\Delta_{21}^2(z=21) \sim 10^5$ mK² for $Q=5\times 10^{-3}$, several orders of magnitude larger than the conventional Λ CDM expectation [57] indicated by the purple band. For $9 \le z \le 30$, 21-cm power spectrum experiments such as MWA [45,50], LOFAR [51,52], and HERA [55,56] have already reported upper limits; we limit ourselves to $z \ge 9$ to avoid uncertainties due to reionization, even though stringent upper limits at z=7.9 have recently been reported by HERA [56].

From comparing the $Q = 2 \times 10^{-2}$ envelopes of both panels of Fig. 1, it is evident that models leading to a maximal global signal absorption feature do not correspond to the largest Δ_{21}^2 values. In the left panel of Fig. 2, we show a scatter plot in the space of $\Delta_{21}^2(k = 0.13)$ Mpc⁻¹ and

 $\langle T_{21} \rangle$ at z = 17, for $m_{\rm m} = 3$ GeV and the experimentally allowed range of Q [29]. Each gray line is a fixed astrophysical model, with varying charge Q. The colored dots indicate the maximal Δ_{21}^2 and minimal $\langle T_{21} \rangle$ across all astrophysical models, for a fixed Q. We see that increasing Q first leads to gradually increasing values of Δ_{21}^2 , before $\langle T_{21} \rangle$ starts decreasing significantly. This behavior stems from the $\sigma \propto v_{\rm rel}^{-4}$ relative velocity dependence of the Rutherford scattering cross section between mDM and baryons; cooling is most efficient for regions where $v_{\rm bC} = 0$, while for higher velocities, less efficient cooling or even heating can take place [22]. This leads to enhanced fluctuations in T_b and hence T_{21} . As Q is increased further, these fluctuations are diminished, since large regions of the IGM—with most values of v_{bC} —experience strong and early cooling; this behavior is reflected in the right panel of Fig. 1, where Δ_{21}^2 begins to decrease for $Q \gtrsim 5 \times 10^{-3}$.

In the same figure, we show the forecast sensitivity of NenuFAR [82] and HERA [27] after 10^3 hours of observation, for $k=0.13~\rm Mpc^{-1}$. We note that the Square Kilometre Array (SKA) is projected to do even better, reaching a sensitivity of around $1~\rm mK^2$ [83]. For many choices of $(Q, m_{\rm m})$, we see that 21-cm power spectrum experiments are sensitive to these models, even though the global signal only has a value of $\langle T_{21} \rangle \approx -200~\rm mK$, only slightly larger than the Λ CDM expectation shown in Fig. 1 [57]. At present, measurements by the SARAS experiment have excluded the central value of the EDGES absorption profile at the 95% confidence level, but with the exclusion likely depending on the signal shape and not just on the amplitude.



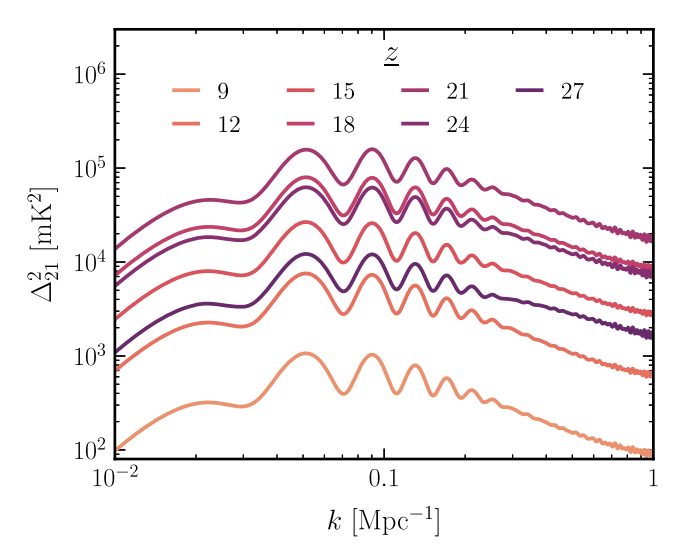


FIG. 2. Left: scatter plot of the global signal and the power spectrum at k = 0.13 Mpc⁻¹ at z = 17, for $m_{\rm m} = 3$ GeV. Each gray line is a fixed astrophysical model with varying charge Q, while the color of each large dot represents a value of Q and indicates the maximum fluctuation and absorption signal for that value. The EDGES central value of $\langle T_{21} \rangle = -500$ mK with its error range is shown for reference (brown, horizontal), although the EDGES profile is ruled out at 95% confidence by SARAS. The projected sensitivities of NenuFAR [82] (green, dotted) and HERA [27] (blue, dotted) with 10^3 hours of observation are shown. Right: the power spectrum as a function of k at various redshifts (colored lines), maximized over both astrophysics and particle physics parameters.

Finally, in the right panel of Fig. 2, we plot the maximum Δ_{21}^2 across all astrophysical and new-physics models parameters, for experimentally relevant values of k and z. Across a broad range of k and z, $\Delta_{21}^2 \gtrsim 10^3$ mK², reaching values as large as $\Delta_{21}^2 \sim 10^5$ mK², exceeding the fiducial expectation from Λ CDM cosmology by several orders of magnitude (see Appendix A for a density plot of Δ_{21}^2 over all relevant values of k and k). Furthermore, large acoustic oscillations are imprinted in the k1 signal through the correlation between k2 and k3. This is currently the only viable new-physics model with large acoustic oscillations in the 21-cm power spectrum, and provides a new-physics target for experiments like NenuFAR and HERA.

VII. CONCLUSION

We studied the 21-cm power spectrum of the two-fluid interacting millicharged DM model first studied in Ref. [29], and found that the model can produce a power spectrum that will be readily detectable in near-future runs of 21-cm power spectrum experiments such as NenuFAR and HERA, and eventually the SKA. Large power spectra are possible even in models in which the predicted global signal is close to the standard Λ CDM range. This model is currently the only viable model which produces a large 21-cm power spectrum with acoustic oscillation features, demonstrating the power of such experiments in searching for new physics. Our results should provide a useful new-physics benchmark for upcoming 21-cm power spectrum experimental results.

While this study has strategically chosen certain astrophysical models to maximize the detection potential of the discussed signal, we acknowledge the importance of expanded parameter exploration and the consideration of more diverse astrophysical models in future research, including those that could potentially diminish the detectability of the signal. Moreover, our treatment of heating is approximate, and we anticipate deviations when the heating and cooling effects of our particle physics model are of a similar order. We recognize the need to address this aspect in more detail in future work, particularly should an anomalously large 21-cm power spectrum be observed. This broader and more refined approach is essential to ensure a comprehensive understanding of the phenomena under study. Likewise, if early signs of our model begin to surface in forthcoming 21-cm power spectrum results, a more comprehensive analysis, such as conducting a Markov chain Monte Carlo, would indeed become an essential step in verifying the validity of our model and its implications.

ACKNOWLEDGMENTS

The authors would like to thank Yacine Ali-Haïmoud, Tomer Volansky and Omer Katz for useful discussions. R. B. acknowledges the support of the Israel Science Foundation (Grant No. 2359/20), the Ambrose Monell Foundation and the Institute for Advanced Study as well as the Vera Rubin Presidential Chair in Astronomy at University of California, Santa Cruz and the Packard Foundation. A.F. was supported by the Royal Society University Research Fellowship. H. L. is supported by NSF Grant No. PHY-2210498, the Department of Energy under Award No. DESC0007968 and the Simons Foundation. The work of N.J.O. was supported in part by the Zuckerman STEM Leadership Program and by the National Science Foundation (NSF) under the Grant No. PHY-1915314. This work was performed in part at the Aspen Center for Physics, which is supported by NSF Grant No. PHY-1607611. This work was also performed using the Princeton Research Computing resources at Princeton University which is a consortium of groups including the Princeton Institute for Computational Science and Engineering and the Princeton University Office of Information Technology's Research Computing department. This research made use of the IPython [84], Jupyter [85], Matplotlib [86], NumPy [87], PYFFTLOG [88–90], SEABORN [91], PANDAS [92], SciPy [93], and TQDM [94] software packages.

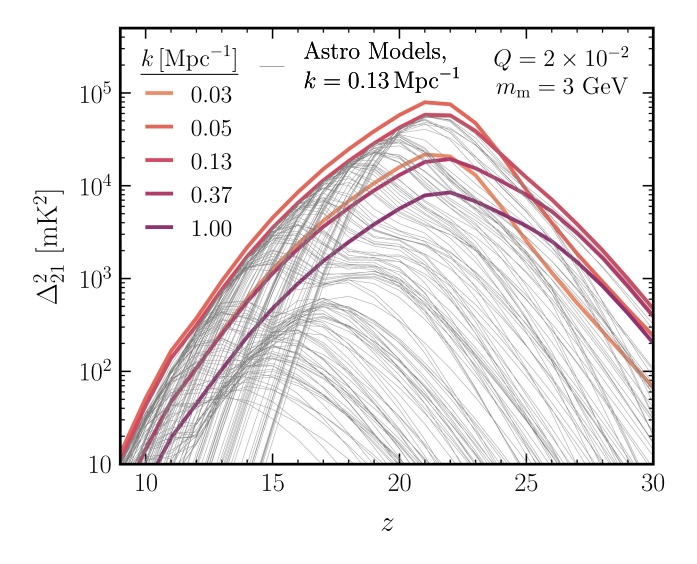
APPENDIX A: SUPPLEMENTAL FIGURES

In the left plot in Fig. 3, we show the maximum envelope of Δ^2_{21} for $m_{\rm m}=3$ GeV and $Q=2\times 10^{-2}$ as a function of redshift for several values of k, including the predicted signals for all astrophysical models with k=0.13 Mpc⁻¹. On the right of Fig. 3, we show contours of $\Delta^2_{T_{21}}(k,z)$ maximized over both astrophysics and particle physics parameters.

APPENDIX B: 21-CM COSMOLOGY FOR HIGH-ENERGY PHYSICISTS

In this appendix, we briefly review the physics of the 21-cm emission in a language familiar to high-energy physicists, and detail the full calculation for obtaining the brightness temperature T_{21} , paying special attention to deriving expressions that are valid even when the spin temperature is comparable to the hyperfine splitting, a scenario that is possible due to the significant cooling of baryons in the two-fluid dark sector model. For an extensive review, we refer the readers to Ref. [5].

Consider a line-of-sight through a large region of space, parametrized by comoving coordinates x and redshift z. Radiation from the CMB with temperature $T_{\gamma}(z)$ is incident on neutral hydrogen or HI gas at x with number density $n_{\rm HI}(x,z)$. Since the 21-cm line is very narrow (it has a decay width of $A_{10}=2.85\times 10^{-15}\,{\rm s}^{-1}$, compared to the energy level separation corresponding to a frequency of $\nu_{10}=1.42$ GHz), we can safely treat all interactions with neutral hydrogen as occurring only when the energy of the photon is exactly given by the hyperfine splitting



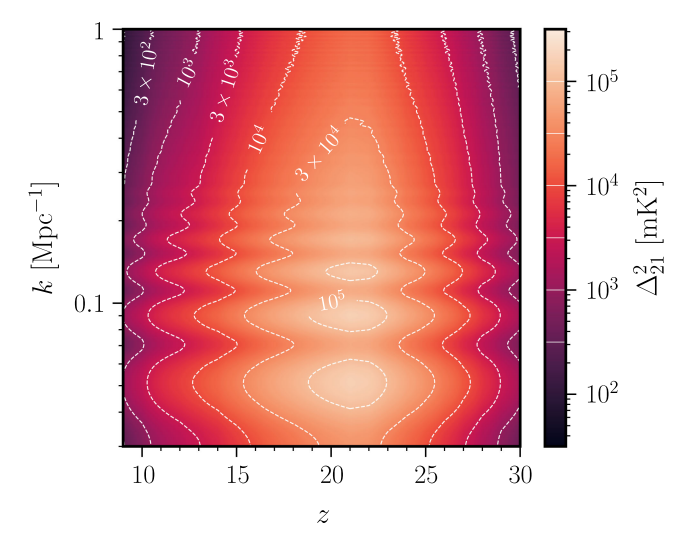


FIG. 3. Left: the maximum envelope of the power spectrum Δ_{21}^2 for $m_{\rm m}=3$ GeV and $Q=2\times 10^{-2}$ as a function of redshift for several values of k (colored lines). The predicted signals for all astrophysical models with k=0.13 Mpc⁻¹ are shown in gray. Right: contours of $\Delta_{T_{21}}^2(k,z)$, maximized over both astrophysics and particle physics parameters.

 $\omega_{10} \equiv 2\pi\nu_{10}$ at each point in z. Photons approaching the point with frequency just above ν_{10} enter with the CMB blackbody intensity $I_{\nu,\mathrm{BB}}(\nu=\nu_{10},T_{\gamma}(z))$, with intensity being defined with respect to frequency $\nu^{.1}$ At this point, 21-cm photons can be absorbed or emitted by the gas, leading to a change in its intensity $\Delta I_{\nu_{10}}(z)$. This change in the intensity with respect to the blackbody is the observable in 21-cm cosmology.

There are three processes at redshift z that contribute to $\Delta I_{\nu_{10}}(z)$: spontaneous emission, absorption and stimulated emission. In the study of radiative transfer, it is conventional to treat absorption and stimulated emission together, while spontaneous emission is regarded as a source term at each point. Under the narrow-width approximation, we can write the absorption cross section as $\sigma_{0\to 1} \equiv S\delta(\omega - \omega_{10})$, where S is a constant, so that the number of photons absorbed per volume per time is simply $n_0(dn_{\gamma}/d\omega)|_{\omega_{10}}S$, where $(dn_{\gamma}/d\omega|_{\omega_{10}})$ is the number density of photons per unit energy at frequency ω_{10} , where n_0 is the number density of neutral hydrogen atoms in the ground state of the hyperfine splitting. Similarly, stimulated emission can be encapsulated in an effective cross section $\sigma_{1\rightarrow0}$ = $R\delta(\omega-\omega_{10})$, and the number of photons emitted by stimulated emission per volume per time is written as $n_1(dn_\gamma/d\omega)|_{\omega_{10}}R$ for another constant R, where n_1 is the number density of neutral hydrogen atoms in the excited state of the hyperfine splitting. Then the usual detailed balance argument used in deriving the Einstein coefficients tells us that in equilibrium at any temperature T,

$$n_1^{\text{eq}} A_{10} + n_1^{\text{eq}} R \frac{dn_{\gamma}^{\text{eq}}}{d\omega}\Big|_{\omega_{10}} = n_0^{\text{eq}} S \frac{dn_{\gamma}^{\text{eq}}}{d\omega}\Big|_{\omega_{10}},$$

where "eq" denotes equilibrium quantities. The various number densities are given by $n_1^{\text{eq}}/n_0^{\text{eq}} = 3e^{-\omega_{10}/T}$, and

$$\frac{dn_{\gamma}^{\text{eq}}}{d\omega}\bigg|_{\omega_{10}} = \frac{\omega_{10}^2}{\pi^2} \frac{1}{e^{\omega_{10}/T} - 1}.$$

Using the fact that detailed balance applies at any temperature, we find the following relationship:

$$R = \frac{S}{3} = \frac{\pi^2}{\omega_{10}^2} A_{10}.$$
 (B1)

We now define the optical depth of a photon passing through the point at redshift z to be

$$\tau(z) = \int dt [n_0(z)S - n_1(z)R] \delta(\omega - \omega_{10})$$

$$= \int dt n_0(z) [1 - e^{-\omega_{10}/T_S(z)}] S\delta(\omega - \omega_{10}), \quad (B2)$$

where we have used the definition of the spin temperature,

$$n_1/n_0 \equiv 3 \exp(-\omega_{10}/T_S).$$
 (B3)

Notice that the optical depth is defined using the net rate of absorption and stimulated emission. As the photon travels through the point at redshift z, it comes into resonance with $\dot{\omega} = H(z)\omega$. We can therefore rewrite the integral in terms of $d\omega = H(z)\omega dt$, and perform the integral to obtain

¹This assumes that the only 21-cm photons passing through this point originate only from the CMB, and that the CMB is a perfect blackbody with no other sources of distortion.

$$\tau(z) = \frac{3\pi^2 A_{10} n_{\rm HI}(z)}{H(z) \omega_{10}^3} \frac{1 - e^{-\omega_{10}/T_{\rm S}(z)}}{1 + 3e^{-\omega_{10}/T_{\rm S}(z)}},$$

with $n_{\rm HI}=n_0+n_1$. In this expression, we have avoided the common approximation $\omega_{10}\ll T_{\rm S}$, since baryonic cooling in our model can lead to very small values of $T_{\rm b}$ and hence $T_{\rm S}$. In the limit $\omega_{10}\ll T_{\rm S}$, owing to the highly populated excited triplet state, the optical depth is small, and is numerically given by [5]

$$\begin{split} \tau(z) &\simeq 9.85 \times 10^{-3} \bigg(\frac{T_{\gamma}(z)}{T_{\rm S}(z)}\bigg) \bigg(\frac{\Omega_{\rm b}h}{0.0327}\bigg) \bigg(\frac{\Omega_{\rm m}}{0.307}\bigg)^{-1/2} \\ &\times \bigg(\frac{1+z}{10}\bigg)^{1/2}. \end{split} \tag{B4}$$

After passing through the gas, the 21-cm intensity changes because of a combination of absorption and stimulated emission—encapsulated by $\tau(z)$ —and spontaneous emission. We can write the change in intensity as

$$\Delta I_{\nu_{10}}(z) = -I_{\nu,\text{BB}}(\nu_{10}, T_{\gamma}(z))[1 - e^{-\tau(z)}] + S(z),$$
 (B5)

where $I_{\nu,\mathrm{BB}}(\nu_{10},z)$ is the incoming intensity of 21-cm CMB blackbody radiation, while S(z) is the contribution from spontaneous emission, which only depends on the properties of neutral hydrogen atoms. We know that in thermal equilibrium, i.e. if the incoming intensity were a perfect blackbody with temperature T_{S} , we must have $\Delta I_{\nu_{10}}(z)=0$. From this, we can conclude that

$$S(z) = I_{\nu, BB}(\nu_{10}, T_S(z))[1 - e^{-\tau(z)}].$$

In radio astronomy, the intensity I_{ν} at a particular frequency ν is often expressed as a brightness temperature Θ instead, with $\Theta(\omega) \equiv 2\pi^2 I_{\nu}/\omega^2$. For a blackbody, the relation between Θ and the thermodynamic temperature T is

$$\Theta(\omega) = T \times \frac{\xi}{e^{\xi} - 1},\tag{B6}$$

where $\xi \equiv \omega/T$, with $\Theta = T$ in the limit $\xi \to 0$. The expression in Eq. (B5) can therefore be written as

$$\Delta\Theta(z) = \left[\frac{\xi(z)}{e^{\xi(z)} - 1} T_{S}(z) - T_{\gamma}(z)\right] [1 - e^{-\tau(z)}],$$

where $\xi(z) \equiv \omega_{10}/T_{\rm S}$, and we have taken $\omega_{10} \ll T_{\gamma}(z)$. Finally, the observed 21-cm brightness temperature is precisely this absorption or emission relative to the background $T_{\gamma}(z)$, redshifted to the present day, i.e.

$$T_{21}(z) = \frac{1}{1+z} \left[\frac{\xi(z)}{e^{\xi(z)} - 1} T_{S}(z) - T_{\gamma}(z) \right] [1 - e^{-\tau(z)}].$$
 (B7)

Once again, we have not taken the usual approximation $\omega_{10} \ll T_{\rm S}(z)$ or equivalently $\xi(z) \ll 1$, since this assumption can be violated with baryonic cooling. Adopting this limit allows one to drop the $\xi(z)/(e^{\xi(z)}-1)$ term, recovering the more usual expression [5].

Other than Λ CDM parameters, the only remaining unknown parameter that determines $T_{21}(z)$ is the spin temperature. T_{S} is determined by a competition between (1) scattering of HI atoms with the CMB, which causes $T_{S} \rightarrow T_{\gamma}$, (2) collisions between HI atoms, which causes $T_{S} \rightarrow T_{b}$, and (3) Ly α scattering, which couples T_{S} to the color temperature of the Ly α photons $T_{S} \rightarrow T_{C}$ through the WF effect [70,71,95]. The spin temperature can be expressed as a weighted mean [71]

$$T_{\rm S}^{-1} = \frac{T_{\gamma}^{-1} + x_c T_{\rm b}^{-1} + x_{\alpha} T_{\rm C}^{-1}}{1 + x_c + x_{\alpha}},\tag{B8}$$

where x_c and x_{α} represent coupling coefficients through collisions and Ly α scattering respectively. The collisional coupling coefficient can be written as [96]

$$x_{c} = \frac{\omega_{10}}{A_{10}T_{\gamma}} \left[\kappa_{1-0}^{HH}(T_{b}) n_{HI} + \kappa_{1-0}^{eH}(T_{b}) n_{e} + \kappa_{1-0}^{pH}(T_{b}) n_{p} \right],$$
(B9)

where n_p and n_e are the number densities of free protons and electrons; the rates κ were calculated and tabulated in Refs. [97–99]. The Ly α coefficient is [1,5]

$$x_{\alpha} = \frac{16\pi^{2}\alpha\omega_{10}}{27A_{10}m_{e}T_{\gamma}}J_{\alpha},$$
 (B10)

where $\alpha \approx 1/137$ is the fine-structure constant, and J_{α} is defined as

$$J_{lpha}=\intrac{d\Omega}{4\pi}rac{I_{
u_{lpha}}}{\omega_{lpha}},$$

where $I_{\nu_{\alpha}}$ is the photon intensity at the Ly α frequency, and $\omega_{\alpha} \approx 10.2$ eV is the Ly α transition energy. Including the effect of atomic recoil during Ly α scattering as well as the possibility of multiple scatterings allows us to write Eq. (B8) as

$$T_{\rm S}^{-1} = \frac{T_{\gamma}^{-1} + x_{\rm tot,eff} T_{\rm b}^{-1}}{1 + x_{\rm tot,eff}},$$
 (B11)

where $x_{\text{tot,eff}} = x_c + x_{\alpha,\text{eff}}$, and

$$x_{\alpha,\text{eff}} \equiv x_{\alpha} \left(1 + \frac{T_{\text{se}}}{T_{\text{b}}} \right)^{-1} \exp \left[-2.06 \left(\frac{\Omega_{\text{b}} h}{0.0327} \right)^{1/3} \right] \times \left(\frac{\Omega_{\text{m}}}{0.307} \right)^{-1/6} \left(\frac{1+z}{10} \right)^{1/2} \left(\frac{T_{\text{b}}}{T_{\text{se}}} \right)^{-2/3} . \tag{B12}$$

In this expression, $T_{\rm se} \equiv m_{\rm H} (\omega_{10}/\omega_{\alpha})^2 \approx 0.402$ K, with $m_{\rm H}$ being the mass of the hydrogen atom [5]. For the results presented in the paper, we adopt 140 phenomenologically viable models of $x_{\alpha}(z)$ from Ref. [57], chosen for particular large values of $x_{\alpha}(z)$ so that $T_{\rm S}$ is coupled strongly to the $T_{\rm b}$, leading to optimistically but realistically large values of $T_{\rm 21}$ that can be potentially probed in near-future 21-cm experiments.

APPENDIX C: DETAILS OF THE POWER SPECTRUM CALCULATION

As discussed in the main paper, the statistics of the baryon-CDM bulk relative velocity $v_{\rm bC}$ fully specifies the statistics of T_{21} in the two-fluid dark sector model. $v_{\rm bC}({\pmb x})$ in this model is a Gaussian random field, as it is in Λ CDM cosmology; it is fully specified by its two-point function $P_v(k)$, defined as $\langle \tilde{v}_{\rm bC}({\pmb k}) \tilde{v}_{\rm bC}({\pmb k}') \rangle = (2\pi)^3 \delta^{(3)}({\pmb k} + {\pmb k}') P_v(k)$, where $\hat{k} \tilde{v}_{\rm bC}({\pmb k}) \equiv \tilde{v}_{\rm bC}({\pmb k})$, the Fourier transform of $v_{\rm bC}({\pmb x})$. In particular, the one-point PDF $f(v_{\rm bC})$ is

$$f(\mathbf{v}_{bC}) = \left(\frac{3}{2\pi v_{rms}^2}\right)^{3/2} \exp\left(-\frac{3v_{bC}^2}{2v_{rms}^2}\right),$$
 (C1)

where $v_{\rm rms} \equiv \langle v_{\rm bC}^2({\bf x}) \rangle^{1/2} \approx 29~{\rm km\,s^{-1}}$ at z=1010. With this expression, we can easily obtain the mean value of T_{21} at redshift $z, \langle T_{21} \rangle (z)$, given any particular astrophysics model or new-physics parameters, by integrating over $v_{\rm bC}$, i.e.

$$\langle T_{21} \rangle (z) = \int d^3 v_{bC} f(v_{bC}) T_{21}(v_{bC}, z).$$
 (C2)

Similarly, the 2PCF is given by

$$\xi_{T_{21}}(\mathbf{x}) = \int d^3 \mathbf{v}_{bC,a} \int d^3 \mathbf{v}_{bC,b} \mathcal{P}(\mathbf{v}_{bC,a}, \mathbf{v}_{bC,b}; \mathbf{x})$$

$$\times \delta_{T_{21}}(\mathbf{v}_{bC,a}) \delta_{T_{21}}(\mathbf{v}_{bC,b}), \tag{C3}$$

where $\delta_{T_{21}} \equiv (T_{21} - \langle T_{21} \rangle)/\langle T_{21} \rangle$ is the spatial fluctuation of T_{21} , and \mathcal{P} is the two-point PDF, i.e. the joint probability density function of 3D velocities at two different points, separated by the vector \mathbf{x} , given by

$$\mathcal{P}(\mathbf{v}_{bC,a}, \mathbf{v}_{bC,b}; \mathbf{x}) = \frac{1}{(2\pi)^3 \sqrt{|\mathbf{C}(\mathbf{x})|}} \exp\left[-\frac{1}{2}\vec{U}^\mathsf{T} \mathbf{C}^{-1}(\mathbf{x})\vec{U}\right],$$
(C4)

where $\vec{U} \equiv (\nu_{bC,a}, \nu_{bC,b})$ is a 6D vector, and C is the covariance matrix for this multivariate Gaussian. To differentiate between different types of quantities, we use bold-face letters to represent 3D vectors, an arrow to indicate 6D vectors, sans-serif font for 6×6 matrices, and underscores for 3×3 matrices. Note that ultimately, after

performing the velocity integrals, $\xi_{T_{21}}$ is only a function of $x \equiv |x|$ in a homogeneous and isotropic Universe.

The covariance matrix of the 6D Gaussian is given by [64,81]

$$\frac{\mathsf{C}(x)}{\sigma_v^2} = \mathbb{1}_{6\times 6} + \begin{pmatrix} 0 & \underline{c}(x) \\ c(x) & 0 \end{pmatrix}. \tag{C5}$$

Here, $\sigma_v^2 \equiv v_{\rm rms}^2/3 = \int d \log k \Delta_v^2(k)$ is the 1D velocity dispersion, with $\Delta_v^2(k) \equiv k^3 P_v(k)/(2\pi^2)$. The elements of the 3×3 matrix \underline{c} are given by

$$\underline{c}(\mathbf{x})_{ij} \equiv \frac{\langle v_{\text{bC}}^{i} v_{\text{bC}}^{j} \rangle(\mathbf{x})}{\sigma_{v}^{2}} = c_{\parallel}(x)\hat{\mathbf{x}}^{i}\hat{\mathbf{x}}^{j} + c_{\perp}(x)(\delta^{ij} - \hat{\mathbf{x}}^{i}\hat{\mathbf{x}}^{j}),$$

$$c_{\parallel}(x) = \frac{1}{v_{\text{rms}}^{2}} \int \frac{dk}{k} \Delta_{v}^{2}(k)[j_{0}(kx) - 2j_{2}(kx)],$$

$$c_{\perp}(x) = \frac{1}{v_{\text{rms}}^{2}} \int \frac{dk}{k} \Delta_{v}^{2}(k)[j_{0}(kx) + j_{2}(kx)],$$
(C6)

where j_{ℓ} are the spherical Bessel functions of order ℓ , i and j denote spatial components, δ^{ij} is the Kronecker delta symbol, and \hat{x} is a unit vector in the direction of x. c_{\parallel} and c_{\perp} give the correlation of the velocity component parallel and perpendicular to the separation vector x respectively. For later use, in a coordinate system where $x = x\hat{z}$, the 3D matrix takes the form

$$\underline{c}(x\hat{z}) = \begin{pmatrix} c_{\parallel} & 0 & 0 \\ 0 & c_{\parallel} & 0 \\ 0 & 0 & c_{\perp} \end{pmatrix}. \tag{C7}$$

Throughout this appendix, we find it convenient to use $u\sigma_v = v_{\rm bC}$ as our integration variable. Using the Fourier transform of a 6D Gaussian, the 2PCF of any function f(v) can be expressed as

$$\xi_f(x) = \int d^3 \mathbf{u}_a \int d^3 \mathbf{u}_b \int \frac{d^3 \mathbf{\omega}_a}{(2\pi)^3} \int \frac{d^3 \mathbf{\omega}_b}{(2\pi)^3} e^{i\mathbf{\omega}_a \cdot \mathbf{u}_a} e^{i\mathbf{\omega}_b \cdot \mathbf{u}_b}$$

$$\times \delta_f(\mathbf{u}_a \sigma_v) \delta_f(\mathbf{u}_b \sigma_v) \tilde{\mathcal{P}}(\mathbf{\omega}_a, \mathbf{\omega}_b; \mathbf{x}), \tag{C8}$$

where $\delta_f \equiv f/\langle f \rangle - 1$, (ω_a, ω_b) are the Fourier transforms of (u_a, ω_b) , and

$$\tilde{\mathcal{P}}(\boldsymbol{\omega}_a, \boldsymbol{\omega}_b; \boldsymbol{x}) = \exp\left[-\frac{1}{2}(\omega_a^2 + \omega_b^2) - \boldsymbol{\omega}_a^T \underline{c}(\boldsymbol{x}) \boldsymbol{\omega}_b\right]. \quad (C9)$$

Since T_{21} is an isotropic function of velocity, integrating over the angles of both d^3u can be performed easily

$$d^{3}\boldsymbol{u}_{a}\frac{d^{3}\boldsymbol{\omega}_{a}}{(2\pi)^{3}}d^{3}\boldsymbol{u}_{b}\frac{d^{3}\boldsymbol{\omega}_{b}}{(2\pi)^{3}}e^{i\boldsymbol{\omega}_{a}\cdot\boldsymbol{u}_{a}}e^{i\boldsymbol{\omega}_{b}\cdot\boldsymbol{u}_{b}}$$

$$=u_{a}^{2}du_{a}\frac{d^{3}\boldsymbol{\omega}_{a}}{2\pi^{2}}u_{b}^{2}du_{b}\frac{d^{3}\boldsymbol{\omega}_{b}}{2\pi^{2}}\frac{\sin(u_{a}\boldsymbol{\omega}_{a})\sin(u_{b}\boldsymbol{\omega}_{b})}{u_{a}\boldsymbol{\omega}_{a}}.$$
 (C10)

We can simplify the nondiagonal part of the Gaussian in Eq. (C9) by noting that

$$\boldsymbol{\omega}_{a}^{T} \underline{c}(\mathbf{x}) \boldsymbol{\omega}_{b} = \omega_{a} |\underline{c}(\mathbf{x}) \boldsymbol{\omega}_{b}| \cos \theta_{a}$$
$$= \omega_{a} \omega_{b} \cos \theta_{a} \cdot R(\mathbf{x}, \cos \theta_{b}), \quad (C11)$$

where θ_a is the angle between ω_a and $\underline{c}\omega_b$, and θ_b is the angle between ω_b and x, and where through Eq. (C7) we have identified

$$R(x,\cos\theta_b) \equiv |\underline{c}(\mathbf{x})\boldsymbol{\omega}_b|$$

$$= \sqrt{c_{\perp}^2(x) + \cos^2\theta_b[c_{\parallel}^2(x) - c_{\perp}^2(x)]}. \quad (C12)$$

This result can be directly computed using the expressions in Eq. (C6).

At this point, we can integrate over the two remaining azimuthal angles and θ_a ; after some algebra, we arrive at

$$\xi_f(x) = \frac{2}{\pi} \int du_1 u_1^2 \int du_2 u_2^2 \cdot \delta_f(u_1 \sigma_v) \delta_f(u_2 \sigma_v)$$

$$\times W(u_1, u_2, x), \tag{C13}$$

with

$$W(u_1, u_2, x) = \frac{1}{u_1 u_2} \int_{-1}^{1} \frac{d \cos \theta_b}{2} \frac{\exp\left[-\frac{1}{2} \frac{u_1^2 + u_2^2}{1 - R^2}\right] \sinh\left[\frac{R u_1 u_2}{1 - R^2}\right]}{R\sqrt{1 - R^2}}.$$
(C14)

Equation (C13) can now be integrated numerically for a given $\delta_{T_{21}}(v_{\text{bC}})$ to obtain the 2PCF, $\xi_{T_{21}}(x)$. Note that the numerical integration that needs to be performed is a 3D integral, which is numerically much simpler to evaluate than the equivalent 4D integral expressions found in Refs. [64,81].

Implementing Eq. (C13) numerically poses some mild numerical challenges. For separations x much shorter than the sound horizon, which sets the typical scale of spatial fluctuations, $c_{\perp}, c_{\parallel} \rightarrow 1$ and $R \rightarrow 1$, and the 3D integral becomes extremely peaked and difficult to evaluate numerically with a regular mesh. On the other hand, for distances much larger than the sound horizon, the correlation between the two points becomes weak; a series expansion in the limit of large x produces a simple expression for $\xi_{T_{21}}$ that is highly accurate, allowing us to avoid performing the relatively expensive numerical integration. We will now discuss the small-x and large-x limits in turn.

1. Small-separation limit

At distances much smaller than the sound horizon, we expect $c_{\parallel}, c_{\perp} \to 1$. To understand what happens in this limit, we first write Eq. (C8) as

$$\xi_f(x) = \int d^3 \mathbf{u}_a \int d^3 \mathbf{u}_b \int \frac{d^3 \mathbf{\omega}_a}{(2\pi)^3} \int \frac{d^3 \mathbf{\omega}_b}{(2\pi)^3} e^{i\mathbf{\omega}_a \cdot \mathbf{u}_a} e^{i\mathbf{\omega}_b \cdot \mathbf{u}_b}$$

$$\times \exp\left[-\frac{1}{2} (\mathbf{\omega}_a + \mathbf{\omega}_b)^2 + \mathbf{\omega}_a^{\mathsf{T}} \underline{d}(x) \mathbf{\omega}_b \right]$$

$$\times \delta_f(u_a \sigma_v) \delta_f(u_b \sigma_v), \tag{C15}$$

with $\underline{d} \equiv 1 - \underline{c}$, which is a small parameter in this limit. We now rewrite $\exp(\boldsymbol{\omega}_a^{\mathsf{T}}\underline{d}(x)\boldsymbol{\omega}_b)$ as derivatives acting on $\exp(i\boldsymbol{\omega}_a \cdot \boldsymbol{u}_a) \exp(i\boldsymbol{\omega}_b \cdot \boldsymbol{u}_b)$, to obtain

$$\xi_{f}(x) = \int d^{3}\boldsymbol{u}_{a} \int d^{3}\boldsymbol{u}_{b} \delta_{f}(\boldsymbol{u}_{a}\boldsymbol{\sigma}_{v}) \delta_{f}(\boldsymbol{u}_{b}\boldsymbol{\sigma}_{v}) \exp[-\partial_{a}^{i}\partial_{b}^{j}\underline{d}_{ij}]$$

$$\times \int \frac{d^{3}\boldsymbol{\omega}_{a}}{(2\pi)^{3}} \int \frac{d^{3}\boldsymbol{\omega}_{b}}{(2\pi)^{3}} e^{i\boldsymbol{\omega}_{a} \cdot \boldsymbol{u}_{a}} e^{i\boldsymbol{\omega}_{b} \cdot \boldsymbol{u}_{b}}$$

$$\times \exp\left[-\frac{1}{2}(\boldsymbol{\omega}_{a} + \boldsymbol{\omega}_{b})^{2}\right], \qquad (C16)$$

where we introduced the notation that ∂_a^i is the partial derivative with respect to the component u_a^i (and likewise for ∂_b^i), and we adopt the Einstein summation convention from here on. The last two integrals are now inverse Fourier transforms that we can evaluate, to obtain

$$\xi_{f}(x) = \int d^{3}\boldsymbol{u}_{a} \int d^{3}\boldsymbol{u}_{b}\delta_{f}(u_{a}\sigma_{v})\delta_{f}(u_{b}\sigma_{v}) \exp[-\partial_{a}^{i}\partial_{b}^{j}\underline{d}_{ij}]$$

$$\times \frac{e^{-u_{b}^{2}/2}}{(2\pi)^{3/2}}\delta_{D}^{(3)}(\boldsymbol{u}_{a}-\boldsymbol{u}_{b})$$

$$= \int d^{3}\boldsymbol{u}_{a} \int d^{3}\boldsymbol{u}_{b}\delta_{D}^{(3)}(\boldsymbol{u}_{a}-\boldsymbol{u}_{b}) \frac{e^{-u_{b}^{2}/2}}{(2\pi)^{3/2}}$$

$$\times \exp[-\partial_{a}^{i}\partial_{b}^{j}\underline{d}_{ij}]\delta_{f}(u_{a}\sigma_{v})\delta_{f}(u_{b}\sigma_{v}), \tag{C17}$$

where in the last line we have performed an integration by parts to move the derivatives over.

We are now ready to expand in terms of the small parameter \underline{d}_{ij} . Expanding the exponential to second order, we have

$$\exp\left[-\partial_a^i \partial_b^j \underline{d}_{ij}\right] \simeq 1 - \partial_a^i \partial_b^j \underline{d}_{ij} + \frac{1}{2} \partial_a^i \partial_b^j \partial_a^k \partial_b^l \underline{d}_{ij} \underline{d}_{kl}. \tag{C18}$$

At leading order, we have

$$\xi_f^{(0)}(x \to 0) = \int d^3 \boldsymbol{u}_a \int d^3 \boldsymbol{u}_b \delta_D^{(3)}(\boldsymbol{u}_a - \boldsymbol{u}_b)$$

$$\times \frac{e^{-u_b^2/2}}{(2\pi)^{3/2}} \delta_f(u_a \sigma_v) \delta_f(u_b \sigma_v)$$

$$= \langle \delta_f^2(v) \rangle, \tag{C19}$$

since the PDF of 3D bulk relative velocities is $g(v)d^3v = (2\pi\sigma_v^2)^{-3/2} \exp[-v^2/(2\sigma_v^2)]d^3v$, with $v = \sigma_v u$.

At the next order, evaluating the derivatives, we find

$$\begin{split} \xi_{f}^{(1)}(x \to 0) &= -d_{ij} \int d^{3}\boldsymbol{u}_{a} \int d^{3}\boldsymbol{u}_{b} \delta_{D}^{(3)}(\boldsymbol{u}_{a} - \boldsymbol{u}_{b}) \\ &\times \frac{e^{-u_{b}^{2}/2}}{(2\pi)^{3/2}} \frac{u_{a}^{i} u_{b}^{j}}{u_{a} u_{b}} \sigma_{v}^{2} \delta_{f}^{\prime}(u_{a} \sigma_{v}) \delta_{f}^{\prime}(u_{b} \sigma_{v}) \\ &= -d_{ij} \int d^{3}\boldsymbol{u}_{a} \frac{e^{-u_{a}^{2}/2}}{(2\pi)^{3/2}} \frac{u_{a}^{i} u_{a}^{j}}{u_{a}^{2}} \sigma_{v}^{2} \delta_{f}^{\prime 2}(u_{a} \sigma_{v}). \end{split} \tag{C20}$$

At this point, we make use of the identity

$$\int d^3 \boldsymbol{u} u^i u^j f(u) = \frac{\delta^{ij}}{3} \int d^3 \boldsymbol{u} u^2 f(u), \qquad (C21)$$

which can be deduced from the fact that the symmetry of the integral makes it proportional to the rank-2 isotropic tensor, i.e. the Kronecker delta function. Putting everything together, we finally obtain

$$\xi_f^{(1)}(x \to 0) = -\frac{1}{3} \underline{d}^i{}_i \sigma_v^2 \langle \delta_f'^2 \rangle = -\frac{1}{3} \text{Tr}[\underline{d}] \sigma_v^2 \langle \delta_f'^2 \rangle, \quad (C22)$$

where Tr is the trace of a matrix.

Finally, at the second order, we first expand the derivatives carefully,

$$\partial_a^i \partial_a^k = \frac{\delta^{ik}}{u_a} \partial_a + \frac{u_a^i u_a^k}{u_a^2} \left(\partial_a^2 - \frac{1}{u_a} \partial_a \right), \qquad (C23)$$

which can be applied to the second-order expression to give

$$\xi_f^{(2)}(x \to 0) = \frac{1}{2} \underline{d}_{ij} \underline{d}_{kl} \int d^3 \boldsymbol{u}_b \frac{e^{-u_b^2/2}}{(2\pi)^{3/2}} \times \left[\left(\frac{\delta^{ik}}{u_b} - \frac{u_b^i u_b^k}{u_b^3} \right) \sigma_v \delta_f'(u_a \sigma_v) + \frac{u_b^i u_b^k}{u_b^2} \sigma_v^2 \delta_f''(u_a \sigma_v) \right] \times (i \to j, k \to l). \quad (C24)$$

To simplify the expression, we apply Eq. (C21), as well as the analogous result at rank 4,

$$\int d^3 \boldsymbol{u} u^i u^j u^k u^l f(u)$$

$$= \frac{1}{15} (\delta_{ij} \delta_{kl} + \delta_{ik} \delta_{jl} + \delta_{il} \delta_{jk}) \int d^3 \boldsymbol{u} u^4 f(u)$$

$$= \frac{1}{15} S_{ijkl} \int d^3 \boldsymbol{u} u^4 f(u), \qquad (C25)$$

to obtain

$$\begin{split} \xi_{f}^{(2)}(x \to 0) &= \frac{1}{2} \underline{d}_{ij} \underline{d}_{kl} \int d^{3} \boldsymbol{u}_{b} \frac{e^{-u_{b}^{2}/2}}{(2\pi)^{3/2}} \left(\left[\frac{\delta^{ik} \delta^{jl}}{3u_{b}^{2}} + \frac{S_{ijkl}}{15u_{b}^{2}} \right] \sigma_{v}^{2} \delta_{f}^{\prime 2} \right. \\ &\quad + 2 \left[\frac{\delta^{ik} \delta^{jl}}{3u_{b}} - \frac{S_{ijkl}}{15u_{b}} \right] \sigma_{v}^{3} \delta_{f}^{\prime} \delta_{f}^{\prime \prime} + \frac{S_{ijkl}}{15} \sigma_{v}^{4} \delta_{f}^{\prime \prime 2} \right) \\ &\quad = \frac{1}{2} \underline{d}_{ij} \underline{d}_{kl} \int d^{3} \boldsymbol{u}_{b} \frac{e^{-u_{b}^{2}/2}}{(2\pi)^{3/2}} \left(\left[\frac{1}{3} \delta^{ik} \delta^{jl} + \frac{2S_{ijkl}}{15u_{b}^{2}} - \frac{S_{ijkl}}{15u_{b}^{2}} \right] \sigma_{v}^{2} \delta_{f}^{\prime 2} + \frac{S_{ijkl}}{15} \sigma_{v}^{4} \delta_{f}^{\prime \prime 2} \right), \end{split}$$
(C26)

where in the last line we have performed an integration by parts. Contracting the indices gives finally

$$\xi_{f}^{(2)}(x \to 0) = \left[3\underline{d}^{ik}\underline{d}_{ik} - \underline{d}^{i}{}_{i}\underline{d}^{k}{}_{k}\right] \frac{\sigma_{v}^{2}\langle\delta_{f}^{\prime2}\rangle}{30} + \frac{1}{30}\left(2\underline{d}^{ik}\underline{d}_{ik} + \underline{d}^{i}{}_{i}\underline{d}^{k}{}_{k}\right) \times \left(2\sigma_{v}^{4}\left\langle\frac{\delta_{f}^{\prime2}}{v_{\rm bc}^{2}}\right\rangle + \sigma_{v}^{4}\langle\delta_{f}^{\prime\prime2}\rangle\right). \tag{C27}$$

The combined expression can then be written as

$$\begin{split} \langle f \rangle^2 \xi_f(x \to 0) &\simeq \langle f^2 \rangle - \langle f \rangle^2 \\ &- \frac{1}{9} \left\{ \mathrm{Tr}[\underline{d}] - \frac{1}{2} \mathrm{Tr}[\underline{d}^2] \right\} \langle (v_{\mathrm{rms}} f')^2 \rangle \\ &+ \frac{1}{270} \left\{ \mathrm{Tr}[\underline{d}]^2 + 2 \mathrm{Tr}[\underline{d}^2] \right\} \\ &\times \left\langle \left(2 \frac{v_{\mathrm{rms}}^2}{v_{\mathrm{bC}}^2} - 3 \right) (v_{\mathrm{rms}} f')^2 + (v_{\mathrm{rms}}^2 f'')^2 \right\rangle. \end{split}$$

$$(C28)$$

2. Large-separation limit

At large separations, both c_{\parallel} and c_{\perp} approach 0. Once again, we can start from Eq. (C8) and write

$$\xi_{f}(x) = \int d^{3}\boldsymbol{u}_{a} \int d^{3}\boldsymbol{u}_{b} \delta_{f}(u_{a}\sigma_{v}) \delta_{f}(u_{b}\sigma_{v}) \exp[\partial_{a}^{i}\partial_{b}^{j}\underline{c}_{ij}]$$

$$\times \int \frac{d^{3}\boldsymbol{\omega}_{a}}{(2\pi)^{3}} \int \frac{d^{3}\boldsymbol{\omega}_{b}}{(2\pi)^{3}} e^{i\boldsymbol{\omega}_{a}\cdot\boldsymbol{u}_{a}} e^{i\boldsymbol{\omega}_{a}\cdot\boldsymbol{u}_{b}} \exp\left[-\frac{1}{2}(\omega_{a}^{2} + \omega_{b}^{2})\right].$$
(C29)

We can immediately take the Fourier transform of the Gaussian to find

$$\xi_{f}(x) = \int d^{3}\mathbf{u}_{a} \int d^{3}\mathbf{u}_{b} \delta_{f}(u_{a}\sigma_{v}) \delta_{f}(u_{b}\sigma_{v})$$

$$\times \exp\left[\partial_{a}^{i} \partial_{b}^{j} \underline{c}_{ij}\right] \frac{e^{-u_{a}^{2}/2}}{(2\pi)^{3/2}} \frac{e^{-u_{b}^{2}/2}}{(2\pi)^{3/2}}.$$
(C30)

At this point, we can expand the exponential in the limit of small \underline{c} , noting that any term with odd derivatives in u_a is zero, since the resulting expression is odd under $u_a \to -u_a$. Because $\langle \delta_f \rangle$ is zero, the leading-order result goes as two powers of \underline{c} :

$$\xi_f^{(1)}(x \to \infty) = \frac{1}{2} \underline{c}_{ij} \underline{c}_{kl} \left(\int d^3 \mathbf{u}_a \delta_f(\mathbf{u}_a \sigma_v) \partial_a^i \partial_a^k \frac{e^{-u_a^2/2}}{(2\pi)^{3/2}} \right) \times (a \to b, i \to j, k \to l). \tag{C31}$$

As in the small-separation limit, we can exploit the symmetry of the integral to rewrite $\partial_a^i \partial_a^k \to \partial_a^2 \delta^{ik}/3$, giving

$$\xi_f^{(1)}(x \to \infty) = \frac{1}{18} \underline{c}^{ik} \underline{c}_{ik} \left(\int d^3 \mathbf{u}_a \delta_f(u_a \sigma_v) \partial_a^2 \frac{e^{-u_a^2/2}}{(2\pi)^{3/2}} \right)^2, \tag{C32}$$

which we can evaluate to obtain

$$\xi_f^{(1)}(x \to \infty) = \frac{1}{2} \text{Tr}[\underline{c}^2] \frac{\langle v^2 \delta_f \rangle^2}{v_{\text{rms}}^4}.$$
 (C33)

At the next order, we have

$$\xi_f^{(2)}(x \to \infty)
= \frac{1}{24} \underline{c}_{ij} \underline{c}_{kl} \underline{c}_{mn} \underline{c}_{pq} \left(\int d^3 \mathbf{u}_a \delta_f(u_a \sigma_v) \partial_a^i \partial_a^k \partial_a^m \partial_a^p \frac{e^{-u_a^2/2}}{(2\pi)^{3/2}} \right)
\times (a \to b, i \to j, k \to l, m \to n, p \to q).$$
(C34)

Once again, we can replace $\partial_a^i \partial_a^k \partial_a^m \partial_a^p \to S^{ikmp} \nabla_a^2 \nabla_a^2 / 15$, where $\nabla_a^2 \equiv \partial_a^i \partial_{a,i}$, leading to

$$\xi_f^{(2)}(x \to \infty)
= \frac{S^{ikmp} S^{jlnq}}{24(15)^2} \underline{c}_{ij} \underline{c}_{kl} \underline{c}_{mn} \underline{c}_{pq}
\times \left(\int d^3 \mathbf{u}_a \delta_f(\mathbf{u}_a \sigma_v) \nabla_a^2 \nabla_a^2 \frac{e^{-u_a^2/2}}{(2\pi)^{3/2}} \right)^2.$$
(C35)

Contracting the tensor indices gives

$$S^{ikmp}S^{jlnq}\underline{c}_{ij}\underline{c}_{kl}\underline{c}_{mn}\underline{c}_{pq} = S^{ikmp}(\underline{c}_{ik}^2\underline{c}_{mp}^2 + \underline{c}_{im}^2\underline{c}_{kp}^2 + \underline{c}_{ip}^2\underline{c}_{km}^2)$$

$$= 3[(\underline{c}^{ik}\underline{c}_{ik})^2 + 2(\underline{c}^2)^{ik}(\underline{c}^2)_{ik}]$$

$$= 3\{\mathrm{Tr}[\underline{c}^2]^2 + 2\mathrm{Tr}[\underline{c}^4]\}. \quad (C36)$$

Evaluating the integral and simplifying leads us to the final expression,

$$\xi_f^{(2)}(x \to \infty) = \frac{1}{8} \left\{ \text{Tr}[\underline{c}^2]^2 + 2 \text{Tr}[\underline{c}^4] \right\} \times \left(\frac{3}{5} \frac{\langle v^4 \delta_f \rangle}{v_{\text{rms}}^4} - 2 \frac{\langle v^2 \delta_f \rangle}{v_{\text{rms}}^2} \right)^2.$$
 (C37)

The final combined result is

$$\xi_f(x \to \infty) \simeq \frac{1}{2} \operatorname{Tr}[\underline{c}^2] \frac{\langle v^2 \delta_f \rangle^2}{v_{\text{rms}}^4} + \frac{1}{8} \left\{ \operatorname{Tr}[\underline{c}^2]^2 + 2 \operatorname{Tr}[\underline{c}^4] \right\}$$

$$\times \left(\frac{3}{5} \frac{\langle v^4 \delta_f \rangle}{v_{\text{rms}}^4} - 2 \frac{\langle v^2 \delta_f \rangle}{v_{\text{rms}}^2} \right)^2, \tag{C38}$$

which to leading order is in agreement with Ref. [81].

3. Velocity correlation functions

Finally, in this section, we compute the correlation functions for powers of v_{bC} , which we denote as v for simplicity in this section. We also write ξ_f in terms of various bias factors multiplying velocity correlation functions, which is a common approximation scheme used in the literature.

The correlation functions for v^2 and v^4 are both simple Gaussian integrals, resulting in

$$\begin{split} \xi_{v^2}(x) &= \frac{2}{9} \operatorname{Tr}[\underline{c}^2], \\ \xi_{v^4}(x) &= 4\xi_{v^2} + \frac{8}{225} \left\{ \operatorname{Tr}[\underline{c}^2]^2 + 2 \operatorname{Tr}[\underline{c}^4] \right\}. \end{split} \tag{C39}$$

Alternatively, these expressions could have been obtained by noting that the large-separation expansion is exact to first order for ξ_{v^2} and to second order for ξ_{v^4} . At large separation, we see that $\xi_{v^4} \simeq 4\xi_{v^2}$ to leading order, in agreement with Eq. (C38). It is common to write the correlation function ξ_f as a bias parameter multiplied by ξ_{v^2} and ξ_{v^4} ; comparing our expressions here and Eq. (C38), we find in the large-separation limit

$$\xi_{f}(x \to \infty) \simeq \frac{9}{4} \left(\frac{\langle v^{2} \delta_{f} \rangle}{\langle v^{2} \rangle} \right)^{2} \xi_{v^{2}}(x)$$

$$- \frac{225}{64} \left(2 \frac{\langle v^{2} \delta_{f} \rangle}{\langle v^{2} \rangle} - \frac{\langle v^{4} \delta_{f} \rangle}{\langle v^{4} \rangle} \right)^{2}$$

$$\times \left[4 \xi_{v^{2}}(x) - \xi_{v^{4}}(x) \right]. \tag{C40}$$

In the small-separation limit, we write $\underline{c} = 1 - \underline{d}$ as before, and noting that $\underline{c}^2 = 1 - 2\underline{d} + \underline{d}^2$, we obtain

$$\xi_{v^2}(x) = \frac{2}{3} - \frac{4}{9} \text{Tr}[\underline{d}] + \frac{2}{9} \text{Tr}[\underline{d}^2],$$
 (C41)

which is an exact expression, while keeping terms up to order \underline{d}^2 , we find

$$\begin{split} \xi_{v^4}(x \to 0) &\simeq \frac{16}{5} - \frac{112}{45} \left(\mathrm{Tr}[\underline{d}] - \frac{1}{2} \mathrm{Tr}[\underline{d}^2] \right) \\ &+ \frac{32}{225} (\mathrm{Tr}[\underline{d}]^2 + 2 \mathrm{Tr}[\underline{d}^2]). \end{split} \tag{C42}$$

The above two expressions are in agreement with Eq. (C28), which we can now rewrite as

$$\bar{\xi}_{f}(x \to 0) \simeq \left(\frac{A}{4} - \frac{7B}{48}\right) \bar{\xi}_{v^{2}}(x) + \frac{5B}{192} \bar{\xi}_{v^{4}}(x),$$

$$\bar{\xi}(x) = \xi(x) - \xi(0), \qquad A = \langle [v_{\text{rms}}f'(v)]^{2} \rangle,$$

$$B = \left\langle \left(2\frac{v_{\text{rms}}^{2}}{v^{2}} - 3\right) [v_{\text{rms}}f'(v)]^{2} + [v_{\text{rms}}^{2}f''(v)]^{2} \right\rangle.$$
(C43)

APPENDIX D: DETAILS OF THE SIMULATIONS

We rely on a large-scale, seminumerical 21-cm code based on Refs. [57,66,76,100]. Driven by the specifications of radio telescopes such as the SKA, the simulation models large cosmic volumes (384 3 comoving Mpc 3) with a resolution of 3 comoving Mpc. The initial conditions for density fields, bulk relative velocities between dark matter and baryons [3,66,101], and IGM temperature are generated at z = 60. The halo abundance is calculated within each resolution element using the approach of Ref. [102], which is based on Refs. [103–105]. The resulting number of halos is biased by the local values of the large-scale density and velocity fields. Subsequently, star formation is derived assuming that every halo with a mass higher than

the star-formation threshold will form stars at a given star-formation efficiency [106], which is a function of halo mass as well as the local value of the Lyman-Werner (LW) radiative background, which suppresses star formation via the molecular-cooling channel [101].

Radiation produced by stars and stellar remnants is propagated taking into account redshifting and absorption in the IGM. We follow the evolution and spatial fluctuations in several key radiative backgrounds: x-rays heat up and mildly ionize the IGM, Ly α photons are responsible for the WF coupling and contribute to IGM heating [57], LW photons affect the efficiency of star formation, and ionizing photons drive the process of reionization. We then compute the 21-cm signal of neutral hydrogen affected by all the sources of light within the light cone. The simulation produces three-dimensional cubes of the fluctuating 21-cm signal at a selection of redshifts, which can be used to calculate $\langle T_{21} \rangle$ and $P_{T_{21}}$.

Since the Universe at the time of primordial star formation is practically observationally unconstrained, we perform multiple simulations, varying several free astrophysical parameters within their allowed ranges [57,107]. The relevant astrophysical parameters include the minimum circular velocity of star-forming halos V_c , the star formation efficiency f_* , the x-ray spectral energy distribution, x-ray heating efficiency f_X , the ionizing efficiency of sources, and the mean free path of ionizing photons. In this paper, we aim to highlight the discovery potential of the two-fluid dark sector model in the 21-cm power spectrum; we therefore take an ensemble of simulations of 140 astrophysical models from this realistic parameter range, chosen to minimize astrophysical heating and maximize Ly α coupling, both of which result in a stronger absorption for T_{21} . Specifically, we choose models where $V_c > 16.5 \text{ km s}^{-1}$, $f_X < 0.001 \text{ and } f_{\text{radio}} < 1$ [63]. Although it is included in the model, the process of reionization has a subdominant impact on the high-redshift signals discussed in this paper.

Piero Madau, Avery Meiksin, and Martin J. Rees, 21-cm tomography of the intergalactic medium at high redshift, Astrophys. J. 475, 429 (1997).

^[2] Abraham Loeb and Matias Zaldarriaga, Measuring the Small—Scale Power Spectrum of Cosmic Density Fluctuations Through 21 cm Tomography Prior to the Epoch of Structure Formation, Phys. Rev. Lett. 92, 211301 (2004).

^[3] Dmitriy Tseliakhovich and Christopher Hirata, Relative velocity of dark matter and baryonic fluids and the formation of the first structures, Phys. Rev. D 82, 083520 (2010).

^[4] Steven R. Furlanetto, S. Peng Oh, and Frank H. Briggs, Cosmology at low frequencies: The 21 cm transition and the high-redshift Universe, Phys. Rep. 433, 181 (2006).

^[5] Rennan Barkana, The rise of the first stars: Supersonic streaming, radiative feedback, and 21-cm cosmology, Phys. Rep. **645**, 1 (2016).

^[6] Michael Sitwell, Andrei Mesinger, Yin-Zhe Ma, and Kris Sigurdson, The imprint of warm dark matter on the cosmological 21-cm signal, Mon. Not. R. Astron. Soc. 438, 2664 (2014).

- [7] Toyokazu Sekiguchi and Hiroyuki Tashiro, Constraining warm dark matter with 21 cm line fluctuations due to minihalos, J. Cosmol. Astropart. Phys. 08 (2014) 007.
- [8] Olof Nebrin, Raghunath Ghara, and Garrelt Mellema, Fuzzy dark matter at cosmic dawn: New 21-cm constraints, J. Cosmol. Astropart. Phys. 04 (2019) 051.
- [9] Julian B. Muñoz, Cora Dvorkin, and Francis-Yan Cyr-Racine, Probing the small-scale matter power spectrum with large-scale 21-cm data, Phys. Rev. D 101, 063526 (2020).
- [10] Dana Jones, Skyler Palatnick, Richard Chen, Angus Beane, and Adam Lidz, Fuzzy dark matter and the 21 cm power spectrum, Astrophys. J. **913**, 7 (2021).
- [11] Selim C. Hotinli, David J. E. Marsh, and Marc Kamionkowski, Probing ultra-light axions with the 21-cm signal during cosmic dawn, Phys. Rev. D **106**, 043529 (2022).
- [12] Jordan Flitter and Ely D. Kovetz, Closing the window on fuzzy dark matter with the 21 cm signal, Phys. Rev. D 106, 063504 (2022).
- [13] Carmelo Evoli, Andrei Mesinger, and Andrea Ferrara, Unveiling the nature of dark matter with high redshift 21 cm line experiments, J. Cosmol. Astropart. Phys. 11 (2014) 024.
- [14] Laura Lopez-Honorez, Olga Mena, Ángeles Moliné, Sergio Palomares-Ruiz, and Aaron C. Vincent, The 21 cm signal and the interplay between dark matter annihilations and astrophysical processes, J. Cosmol. Astropart. Phys. 08 (2016) 004.
- [15] Guido D'Amico, Paolo Panci, and Alessandro Strumia, Bounds on Dark Matter Annihilations from 21 cm Data, Phys. Rev. Lett. **121**, 011103 (2018).
- [16] Hongwan Liu and Tracy R. Slatyer, Implications of a 21-cm signal for dark matter annihilation and decay, Phys. Rev. D 98, 023501 (2018).
- [17] Steven Clark, Bhaskar Dutta, Yu Gao, Yin-Zhe Ma, and Louis E. Strigari, 21 cm limits on decaying dark matter and primordial black holes, Phys. Rev. D **98**, 043006 (2018).
- [18] Kingman Cheung, Jui-Lin Kuo, Kin-Wang Ng, and Yue-Lin Sming Tsai, The impact of EDGES 21-cm data on dark matter interactions, Phys. Lett. B **789**, 137 (2019).
- [19] Andrea Mitridate and Alessandro Podo, Bounds on dark matter decay from 21 cm line, J. Cosmol. Astropart. Phys. 05 (2018) 069.
- [20] Rennan Barkana, Possible interaction between baryons and dark-matter particles revealed by the first stars, Nature (London) 555, 71 (2018).
- [21] Hiroyuki Tashiro, Kenji Kadota, and Joseph Silk, Effects of dark matter-baryon scattering on redshifted 21 cm signals, Phys. Rev. D **90**, 083522 (2014).
- [22] Julian B. Muñoz, Ely D. Kovetz, and Yacine Ali-Haïmoud, Heating of baryons due to scattering with dark matter during the dark ages, Phys. Rev. D **92**, 083528 (2015).
- [23] Julian B. Muñoz and Abraham Loeb, A small amount of mini-charged dark matter could cool the baryons in the early Universe, Nature (London) 557, 684 (2018).
- [24] Rennan Barkana, Nadav Joseph Outmezguine, Diego Redigolo, and Tomer Volansky, Strong constraints on light dark matter interpretation of the edges signal, Phys. Rev. D 98, 103005 (2018).

- [25] Anastasia Fialkov, Rennan Barkana, and Aviad Cohen, Constraining Baryon–Dark Matter Scattering with the Cosmic Dawn 21-cm Signal, Phys. Rev. Lett. 121, 011101 (2018).
- [26] Asher Berlin, Dan Hooper, Gordan Krnjaic, and Samuel D. McDermott, Severely Constraining Dark Matter Interpretations of the 21-cm Anomaly, Phys. Rev. Lett. 121, 011102 (2018).
- [27] Julian B. Muñoz, Cora Dvorkin, and Abraham Loeb, 21-cm Fluctuations from Charged Dark Matter, Phys. Rev. Lett. 121, 121301 (2018).
- [28] Ely D. Kovetz, Vivian Poulin, Vera Gluscevic, Kimberly K. Boddy, Rennan Barkana, and Marc Kamionkowski, Tighter limits on dark matter explanations of the anomalous EDGES 21 cm signal, Phys. Rev. D 98, 103529 (2018).
- [29] Hongwan Liu, Nadav Joseph Outmezguine, Diego Redigolo, and Tomer Volansky, Reviving millicharged dark matter for 21-cm cosmology, Phys. Rev. D 100, 123011 (2019).
- [30] Cyril Creque-Sarbinowski, Lingyuan Ji, Ely D. Kovetz, and Marc Kamionkowski, Direct millicharged dark matter cannot explain the EDGES signal, Phys. Rev. D **100**, 023528 (2019).
- [31] Amin Aboubrahim, Pran Nath, and Zhu-Yao Wang, A cosmologically consistent millicharged dark matter solution to the edges anomaly of possible string theory origin, J. High Energy Phys. 12 (2021) 148.
- [32] Peter Adshead, Pranjal Ralegankar, and Jessie Shelton, Dark radiation constraints on portal interactions with hidden sectors, J. Cosmol. Astropart. Phys. 09 (2022) 056.
- [33] Judd D. Bowman, Alan E. E. Rogers, Raul A. Monsalve, Thomas J. Mozdzen, and Nivedita Mahesh, An absorption profile centred at 78 megahertz in the sky-averaged spectrum, Nature (London) 555, 67 (2018).
- [34] Saurabh Singh, Jishnu Nambissan T., Ravi Subrahmanyan, N. Udaya Shankar, B. S. Girish, A. Raghunathan, R. Somashekar, K. S. Srivani, and Mayuri Sathyanarayana Rao, On the detection of a cosmic dawn signal in the radio background, Nat. Astron. 6, 607 (2022).
- [35] Richard F. Bradley, Keith Tauscher, David Rapetti, and Jack O. Burns, A ground plane artifact that induces an absorption profile in averaged spectra from global 21-cm measurements—with possible application to EDGES, Astrophys. J. 874, 153 (2019).
- [36] Saurabh Singh and Ravi Subrahmanyan, The redshifted 21-cm signal in the EDGES low-band spectrum, Astrophys. J. **880**, 26 (2019).
- [37] Marta Spinelli, Gianni Bernardi, and Mario G. Santos, On the contamination of the global 21-cm signal from polarized foregrounds, Mon. Not. R. Astron. Soc. 489, 4007 (2019).
- [38] M. Spinelli, G. Kyriakou, G. Bernardi, P. Bolli, L. J. Greenhill, A. Fialkov, and H. Garsden, Antenna beam characterization for the global 21-cm experiment LEDA and its impact on signal model parameter reconstruction, Mon. Not. R. Astron. Soc. **515**, 1580 (2022).
- [39] Richard Hills, Girish Kulkarni, P. Daniel Meerburg, and Ewald Puchwein, Concerns about modelling of the EDGES data, Nature (London) **564**, E32 (2018).

- [40] L. Philip, Z. Abdurashidova, H. C. Chiang, N. Ghazi, A. Gumba, H. M. Heilgendorff, J. M. Jáuregui-García, K. Malepe, C. D. Nunhokee, J. Peterson, J. L. Sievers, V. Simes, and R. Spann, Probing radio intensity at high-Z from Marion: 2017 instrument, J. Astron. Instrum. 08, 1950004 (2019).
- [41] Tabitha C. Voytek, Aravind Natarajan, José Miguel Jáuregui García, Jeffrey B. Peterson, and Omar López-Cruz, Probing the dark ages at *z* ~ 20: The SCI-HI 21 cm all-sky spectrum experiment, Astrophys. J. Lett. **782**, L9 (2014).
- [42] E. de Lera Acedo *et al.*, The REACH radiometer for detecting the 21-cm hydrogen signal from redshift $z \approx 7.5$ –28, Nat. Astron. **6**, 984 (2022).
- [43] Adrian Liu, H. Cynthia Chiang, Abigail Crites, Jonathan Sievers, and Renée Hložek, High-redshift 21 cm cosmology in Canada, arXiv:1910.03153.
- [44] Gregory Paciga *et al.*, A refined foreground-corrected limit on the HI power spectrum at z = 8.6 from the GMRT epoch of reionization experiment, Mon. Not. R. Astron. Soc. **433**, 639 (2013).
- [45] Joshua S. Dillon *et al.*, Overcoming real-world obstacles in 21 cm power spectrum estimation: A method demonstration and results from early murchison widefield array data, Phys. Rev. D **89**, 023002 (2014).
- [46] A. P. Beardsley *et al.*, First season MWA EoR power spectrum results at redshift 7, Astrophys. J. 833, 102 (2016).
- [47] W. Li et al., First season MWA phase II EoR power spectrum results at redshift 7, Astrophys. J. 887, 141 (2019).
- [48] N. Barry *et al.*, Improving the epoch of reionization power spectrum results from Murchison widefield array season 1 observations, Astrophys. J. **884**, 1 (2019).
- [49] Cathryn M. Trott *et al.*, Deep multiredshift limits on epoch of reionization 21 cm power spectra from four seasons of Murchison Widefield Array observations, Mon. Not. R. Astron. Soc. 493, 4711 (2020).
- [50] S. Yoshiura *et al.*, A new MWA limit on the 21 cm power spectrum at redshifts ~13–17, Mon. Not. R. Astron. Soc. **505**, 4775 (2021).
- [51] A. H. Patil *et al.*, Upper limits on the 21-cm Epoch of Reionization power spectrum from one night with LOFAR, Astrophys. J. **838**, 65 (2017).
- [52] F. G. Mertens *et al.*, Improved upper limits on the 21-cm signal power spectrum of neutral hydrogen at $z \approx 9.1$ from LOFAR, Mon. Not. R. Astron. Soc. **493**, 1662 (2020).
- [53] Matthew Kolopanis *et al.*, A simplified, lossless re-analysis of PAPER-64, Astrophys. J. **883**, 133 (2019).
- [54] Hugh Garsden, Lincoln Greenhill, Gianni Bernardi, Anastasia Fialkov, Daniel C. Price, Daniel Mitchell, Jayce Dowell, Marta Spinelli, and Frank K. Schinzel, A 21-cm power spectrum at 48 MHz, using the owens valley long wavelength array, Mon. Not. R. Astron. Soc. 506, 5802 (2021).
- [55] Zara Abdurashidova et al. (HERA Collaboration), First results from HERA phase I: Upper limits on the epoch of reionization 21 cm power spectrum, Astrophys. J. 925, 221 (2022).

- [56] Zara Abdurashidova *et al.* (HERA Collaboration), Improved constraints on the 21 cm EoR power spectrum and the X-ray heating of the IGM with HERA phase I observations, Astrophys. J. **945**, 124 (2023).
- [57] Itamar Reis, Anastasia Fialkov, and Rennan Barkana, The subtlety of Ly-a photons: Changing the expected range of the 21-cm signal, Mon. Not. R. Astron. Soc. 506, 5479 (2021).
- [58] Sourabh Paul, Mario G. Santos, Zhaoting Chen, and Laura Wolz, A first detection of neutral hydrogen intensity mapping on Mpc scales at $z \approx 0.32$ and $z \approx 0.44$, arXiv: 2301.11943.
- [59] Chang Feng and Gilbert Holder, Enhanced global signal of neutral hydrogen due to excess radiation at cosmic dawn, Astrophys. J. Lett. 858, L17 (2018).
- [60] A. Ewall-Wice, T.-C. Chang, J. Lazio, O. Dore, M. Seiffert, and R. A. Monsalve, Modeling the radio background from the first black holes at cosmic dawn: Implications for the 21 cm absorption amplitude, Astrophys. J. 868, 63 (2018).
- [61] Maxim Pospelov, Josef Pradler, Joshua T. Ruderman, and Alfredo Urbano, Room for New Physics in the Rayleigh-Jeans Tail of the Cosmic Microwave Background, Phys. Rev. Lett. 121, 031103 (2018).
- [62] Anastasia Fialkov and Rennan Barkana, Signature of excess radio background in the 21-cm global signal and power spectrum, Mon. Not. R. Astron. Soc. **486**, 1763 (2019).
- [63] Itamar Reis, Anastasia Fialkov, and Rennan Barkana, High-redshift radio galaxies: A potential new source of 21-cm fluctuations, Mon. Not. R. Astron. Soc. 499, 5993 (2020).
- [64] Neal Dalal, Ue-Li Pen, and Uros Seljak, Large-scale BAO signatures of the smallest galaxies, J. Cosmol. Astropart. Phys. 11 (2010) 007.
- [65] Matthew McQuinn and Ryan M. O'Leary, The impact of the supersonic baryon-dark matter velocity difference on the $z \sim 20.21$ cm background, Astrophys. J. **760**, 3 (2012).
- [66] Eli Visbal, Rennan Barkana, Anastasia Fialkov, Dmitriy Tseliakhovich, and Christopher Hirata, The signature of the first stars in atomic hydrogen at redshift 20, Nature (London) **487**, 70 (2012).
- [67] Julian B. Muñoz, Robust velocity-induced acoustic oscillations at cosmic dawn, Phys. Rev. D 100, 063538 (2019).
- [68] Roland de Putter, Olivier Doré, Jérôme Gleyzes, Daniel Green, and Joel Meyers, Dark Matter Interactions, Helium, and the Cosmic Microwave Background, Phys. Rev. Lett. **122**, 041301 (2019).
- [69] Kimberly K. Boddy, Vera Gluscevic, Vivian Poulin, Ely D. Kovetz, Marc Kamionkowski, and Rennan Barkana, Critical assessment of CMB limits on dark matter-baryon scattering: New treatment of the relative bulk velocity, Phys. Rev. D 98, 123506 (2018).
- [70] S. A. Wouthuysen, On the excitation mechanism of the 21-cm (radio-frequency) interstellar hydrogen emission line, Astron. J. **57**, 31 (1952).
- [71] George B. Field, Excitation of the hydrogen 21-cm line, Proc. IRE **46**, 240 (1958).

- [72] Cora Dvorkin, Kfir Blum, and Marc Kamionkowski, Constraining dark matter-baryon scattering with linear cosmology, Phys. Rev. D 89, 023519 (2014).
- [73] Weishuang Linda Xu, Cora Dvorkin, and Andrew Chael, Probing sub-GeV dark matter-baryon scattering with cosmological observables, Phys. Rev. D 97, 103530 (2018).
- [74] Vera Gluscevic and Kimberly K. Boddy, Constraints on Scattering of keV–TeV Dark Matter with Protons in the Early Universe, Phys. Rev. Lett. 121, 081301 (2018).
- [75] Bob Holdom, Two U(1)'s and epsilon charge shifts, Phys. Lett. **166B**, 196 (1986).
- [76] Anastasia Fialkov, Rennan Barkana, Arazi Pinhas, and Eli Visbal, Complete history of the observable 21-cm signal from the first stars during the pre-reionization era, Mon. Not. R. Astron. Soc. 437, L36 (2014).
- [77] Xue-Lei Chen and Jordi Miralda-Escude, The spin—kinetic temperature coupling and the heating rate due to Lyαscattering before reionization: Predictions for 21 cm emission and absorption, Astrophys. J. **602**, 1 (2004).
- [78] Leonid Chuzhoy and Paul R. Shapiro, Uv pumping of hyperfine transitions in the light elements, with application to 21-cm hydrogen and 92-cm deuterium lines from the early universe, Astrophys. J. 651, 1 (2006).
- [79] Steven R. Furlanetto and Jonathan R. Pritchard, The scattering of Lyman-series photons in the intergalactic medium, Mon. Not. R. Astron. Soc. 372, 1093 (2006).
- [80] Tejaswi Venumadhav, Liang Dai, Alexander Kaurov, and Matias Zaldarriaga, Heating of the intergalactic medium by the cosmic microwave background during cosmic dawn, Phys. Rev. D 98, 103513 (2018).
- [81] Yacine Ali-Haïmoud, P. Daniel Meerburg, and Sihan Yuan, New light on 21 cm intensity fluctuations from the dark ages, Phys. Rev. D 89, 083506 (2014).
- [82] F. G. Mertens, B. Semelin, and L. V. E. Koopmans, Exploring the cosmic dawn with NenuFAR, in *Semaine de l'astrophysique française 2021* (Société Française d'Astronomie et d'Astrophysique (SF2A), Paris, France, 2021), arXiv:2109.10055.
- [83] L. Koopmans *et al.*, The cosmic dawn and epoch of reionisation with SKA, Proc. Sci., AASKA14 (**2015**) 001.
- [84] Fernando Perez and Brian E. Granger, IPython: A system for interactive scientific computing, Comput. Sci. Eng. 9, 21 (2007).
- [85] Thomas Kluyver *et al.*, Jupyter notebooks—a publishing format for reproducible computational workflows, in *ELPUB* (University of Southampton, Southampton, United Kingdom, 2016).
- [86] J. D. Hunter, Matplotlib: A 2d graphics environment, Comput. Sci. Eng. 9, 90 (2007).
- [87] Charles R. Harris *et al.*, Array programming with NumPy, Nature (London) **585**, 357 (2020).
- [88] James D Talman, Numerical fourier and bessel transforms in logarithmic variables, J. Comput. Phys. 29, 35 (1978).
- [89] A. J. S. Hamilton, Uncorrelated modes of the nonlinear power spectrum, Mon. Not. R. Astron. Soc. 312, 257 (2000).

- [90] Dieter Werthmüller, prisae/pyfftlog: First packaged release (2020).
- [91] Michael Waskom et al., mwaskom/seaborn: v0.8.1 (september 2017) (2017).
- [92] Wes McKinney, Data structures for statistical computing in python, in *Proceedings of the 9th Python in Science Conference*, *Austin, Texas*, edited by Stéfan van der Walt and Jarrod Millman (2010), pp. 51–56, https://conference.scipy.org/proceedings/scipy2010/pdfs/proceedings.pdf.
- [93] Pauli Virtanen et al., SciPy 1.0: Fundamental algorithms for scientific computing in Python, Nat. Methods 17, 261 (2020).
- [94] Casper O da Costa-Luis, TQDM: A fast, extensible progress meter for Python and CLI, J. Open Source Softwaare 4, 1277 (2019).
- [95] George B. Field, The time relaxation of a resonance-line profile, Astrophys. J. **129**, 551 (1959).
- [96] Jonathan R. Pritchard and Abraham Loeb, 21-cm cosmology, Rep. Prog. Phys. **75**, 086901 (2012).
- [97] B. Zygelman, Hyperfine level-changing collisions of hydrogen atoms and tomography of the dark age universe, Astrophys. J. 622, 1356 (2005).
- [98] Steven Furlanetto and Michael Furlanetto, Spin exchange rates in electron-hydrogen collisions, Mon. Not. R. Astron. Soc. 374, 547 (2007).
- [99] Steven Furlanetto and Michael Furlanetto, Spin exchange rates in proton-hydrogen collisions, Mon. Not. R. Astron. Soc. 379, 130 (2007).
- [100] Anastasia Fialkov, Rennan Barkana, and Eli Visbal, The observable signature of late heating of the universe during cosmic reionization, Nature (London) 506, 197 (2014).
- [101] Anastasia Fialkov, Rennan Barkana, Eli Visbal, Dmitriy Tseliakhovich, and Christopher M. Hirata, The 21-cm signature of the first stars during the Lyman-Werner feedback era, Mon. Not. R. Astron. Soc. 432, 2909 (2013).
- [102] Rennan Barkana and Abraham Loeb, Unusually large fluctuations in the statistics of galaxy formation at high redshift, Astrophys. J. 609, 474 (2004).
- [103] William H. Press and Paul Schechter, Formation of galaxies and clusters of galaxies by selfsimilar gravitational condensation, Astrophys. J. 187, 425 (1974).
- [104] J. R. Bond, S. Cole, G. Efstathiou, and N. Kaiser, Excursion set mass functions for hierarchical Gaussian fluctuations, Astrophys. J. 379, 440 (1991).
- [105] Ravi K. Sheth and Giuseppe Tormen, Large scale bias and the peak background split, Mon. Not. R. Astron. Soc. 308, 119 (1999).
- [106] Aviad Cohen, Anastasia Fialkov, Rennan Barkana, and Raul Monsalve, Emulating the global 21-cm signal from cosmic dawn and reionization, Mon. Not. R. Astron. Soc. 495, 4845 (2020).
- [107] Aviad Cohen, Anastasia Fialkov, and Rennan Barkana, Charting the parameter space of the 21-cm power spectrum, Mon. Not. R. Astron. Soc. 478, 2193 (2018).